NPL
National Physical Laboratory

NPL REPORT MAT 91

IN SITU CRACK GROWTH MEASUREMENTS OF ATMOSPHERIC INDUCED STRESS CORROSION CRACKING OF 316L STAINLESS STEEL FOR HAW CONTAINERS

YUE ZHANG, ANGUS COOK, CRISTIANO PADOVANI, SHENGQI ZHOU, ALAN TURNBULL

FEBURARY 2020

In Situ Crack Growth Rate Measurements of Atmospheric Induced Stress Corrosion Cracking of 316L Stainless Steel for HAW Containers

Yue Zhang[1], Angus Cook[2], Cristiano Padovani[2], Shengqi Zhou[1], Alan Turnbull[1]

[1]Electrochemistry Group, National Physical Laboratory, Teddington, TW11 0LW
[2]Wood Technical Consulting Solutions, Harwell, OX11 0GD

© NPL Management Limited, 2020

ISSN 1754-2979

https://doi.org/10.47120/npl.MAT91

National Physical Laboratory
Hampton Road, Teddington, Middlesex, TW11 0LW

Extracts from this report may be reproduced provided the source is acknowledged and the extract is not taken out of context.

Approved on behalf of NPLML by
Gareth Hinds, Science Area Leader, Electrochemistry Group.

EXECUTIVE SUMMARY

Prior to the operation of a geological disposal facility (GDF), the UK's higher activity radioactive waste (HAW) is currently housed in interim surface storage facilities, generally within thin-walled (2.3 mm to 6 mm thickness) containers which are commonly fabricated from 316L stainless steel [1, 2]. It is important to ensure the integrity of the containers during this interim storage phase, which is envisaged to be at least several decades [1], as well as during the subsequent operational phase of the GDF, which may also last several decades. As the interim storage facilities in the UK are often located close to a marine environment, there is a concern that the deposition of chloride-containing aerosols poses a risk of localised corrosion developing on the stainless steel containers, which in the presence of surface tensile residual stress could potentially lead to stress corrosion cracking (SCC).

The main goal of this project is to refine understanding of the durability of stainless steel HAW containers in chloride-containing atmospheres by obtaining quantitative data for stress corrosion crack growth rates as a function of RH under well-defined temperature and salt deposit conditions. The crack propagation rate in 316L stainless steel under atmospheric exposure conditions was measured in situ by a direct current potential drop (DCPD) method. Adopting a procedure used successfully in other applications, dogbone test specimens were pre-pitted and pre-cracked to different initial crack lengths to explore the sensitivity of the crack propagation rate to crack size. An additional specimen was pre-pitted but not pre-cracked. The SCC testing was carried out at an applied stress of 1.1 $\sigma_{0.2}$ with a chloride deposition density of approximately 100 µg/cm^2 deposited as $MgCl_2$ from solution. Atmospheric conditions were maintained at 40 °C with an initial relative humidity (RH) of 40% RH, followed by an increase to 60% RH then 80% RH, and finally a decrease to 60% RH. The total exposure period was about 6500 h (about 9 months).

Stress corrosion crack growth was observed but not consistently for every specimen. SCC and stress corrosion crack growth rates were most significant in situations where cracks evolved from pits formed during the test rather than from the pre-cracks. In the latter cases, SCC occurred only in response to a system perturbation and then only for one specimen. The stress corrosion crack growth rates decreased with increasing RH, likely as a result of solution dilution. In different RH regimes, specific SCC propagation rates were measured as follows:

- At 40% RH, the growth rates attained values of 10^{-10} m/s (3.2 mm/year)
- When increasing the RH from 40% to 60%, the growth rate decreased to about 10^{-11} m/s (320 µm/year) over a period of about 2.5 months
- Upon increasing the RH to 80% the growth rate decreased to about 10^{-12} m/s (32 µm/year) after 2 months
- When decreasing the RH from 80% to 60% the growth rate increased to about $3\text{-}5\times10^{-12}$ m/s (128-192 µm/year) after 2 months

Glossary of terms

Crack surface length	$2c$
Final crack surface length	$2c_f$
Initial crack surface length	$2c_i$
Crack depth	a
Crack aspect ratio (depth / half surface length)	a/c
Final crack depth	a_f
Initial crack depth	a_i
Chloride Deposition Density	CDD
Direct Current Potential Drop	DCPD
Geological Disposal Facility	GDF
Higher Activity Radioactive Waste	HAW
Nominal Stress Intensity Factor	K
Relative Humidity	RH
Stress Corrosion Cracking	SCC
Scanning Electron Microscopy	SEM
X-Ray Diffraction	XRD
0.2% proof stress	$\sigma_{0.2}$

CONTENTS

1 INTRODUCTION

Prior to the operation of a geological disposal facility (GDF), the UK's higher activity radioactive waste (HAW) is currently housed in interim surface storage facilities, generally within thin-walled (2.3 mm to 6 mm thickness) containers which are commonly fabricated from 316L stainless steel [1, 2]. It is important to ensure the integrity of the containers during this interim storage phase, which is envisaged to be at least several decades [1], as well as during the subsequent operational phase of the GDF, which may also last several decades. As the interim storage facilities in the UK are often located close to a marine environment, there is a concern that the deposition of chloride-containing aerosols poses a risk of localised corrosion developing on the stainless steel containers, which in the presence of surface tensile residual stress could potentially lead to stress corrosion cracking (SCC).

As part of a previous research programme, a parametric model to assess the corrosion behaviour of stainless steel containers over their operational lifetime (including both interim-storage and GDF operation) was developed, with the intention of assisting store operators in understanding the likely effects of different storage environments on the containers [3]. The model was called the Atmospheric Corrosion of Stainless Steel in Stores (ACSIS) model, and combined information on likely temperature and humidity behaviour within stores, contaminating salt speciation and wetting behaviour, and corrosion mechanisms and behaviours to predict the extent of corrosion processes on containers.

During the previous programme it was found that, while data were available to parameterise the conditions required for the initiation of SCC, robust data were not available to parameterise the propagation rates of SCC, and any environmental dependence thereof. Based on this, the model was developed to a stage whereby SCC behaviour could be reasonably simulated up to initiation, but placeholder behaviour was used for the propagation (i.e. instant growth to a given depth, with no further growth).

This current work is part of a larger programme aimed at refining the understanding of the behaviour of HAW packages during storage, and using this understanding to further develop the ACSIS model. The main goal of the current work is to obtain quantitative data for crack growth rates in stainless steel as a function of RH under well-defined temperatures and salt deposit conditions. Based on information available to date, the testing conditions used in this programme are expected to be moderately severe relative to real storage environments and designed to yield upper-bound SCC propagation rates.

Specifically, the crack growth rate in 316L stainless steel specimens with a chloride deposition density (CDD) of 100 μg/cm^2 deposited with $MgCl_2$ from solution was measured in situ by a direct current potential drop (DCPD) method at a constant temperature of 40 °C and at varying RH conditions (initially 40% followed by an increase to 60%, then 80%, and finally a decrease to 60%). Specimens were pre-cracked to varying depth to explore the sensitivity of the crack propagation rate to crack size. The crack precursor also provides a known crack geometry, which is used in the analytical model for converting in situ DCPD measurement to crack size.

2 TEST METHODOLOGY

2.1.1 Materials and Specimens

2.1.2 Material composition and mechanical properties

The testing material was 316L stainless steel (SS) (noted as AFUU hereafter) rolled plate provided by Wood Nuclear Ltd. Chemical analysis data using inductively coupled plasma atomic emission spectroscopy (ICP-OES) and mechanical properties data of the material were provided by Wood Nuclear Ltd and are summarised in and Table 2 respectively.

Table 1. Average chemical composition (via ICP-OES) of 316L SS specimens (n=3).

C	Si	Mn	Ni	Cr	Mo	S	P	Fe
0.024	0.43	1.28	9.90	16.67	2.03	0.003	0.039	balance

Table 2. Mechanical properties of the 316L SS in the long transverse direction (across the width of the rolled material) at room temperature (sourced from manufacturer's certificates). $\sigma_{0.2}$ is 0.2% of the proof stress; $\sigma_{1.0}$ is 1% of the proof stress; UTS is the ultimate tensile strength.

$\sigma_{0.2}$ /MPa	$\sigma_{1.0}$ /MPa	UTS /MPa	Elongation to failure /%
328	368	629	56

2.1.3 Specimens

Flat dogbone tensile specimens were fabricated from the 316L SS rolled plate with a gauge length of 20 mm, width of 8 mm and thickness of 2.8 mm (Figure 1). The rolling direction was in the transverse direction of the specimen (Figure 1). The specimens were ground to a P1200 surface finish, which gives an average surface roughness R_a < 0.1 µm. Freshly ground specimens were then sonicated in deionised water, then methanol and finally acetone before drying in laboratory ambient air. The residual stress after grinding was measured by X-Ray Diffraction (XRD); the data are summarised in Table 3. For the wet-ground surface, the residual stress was always compressive, with a maximum magnitude of 195 MPa in the rolling direction of the material. Significant relaxation of this initial residual stress is expected in response to plastic flow and creep (see later) upon loading beyond yield prior to the SCC testing.

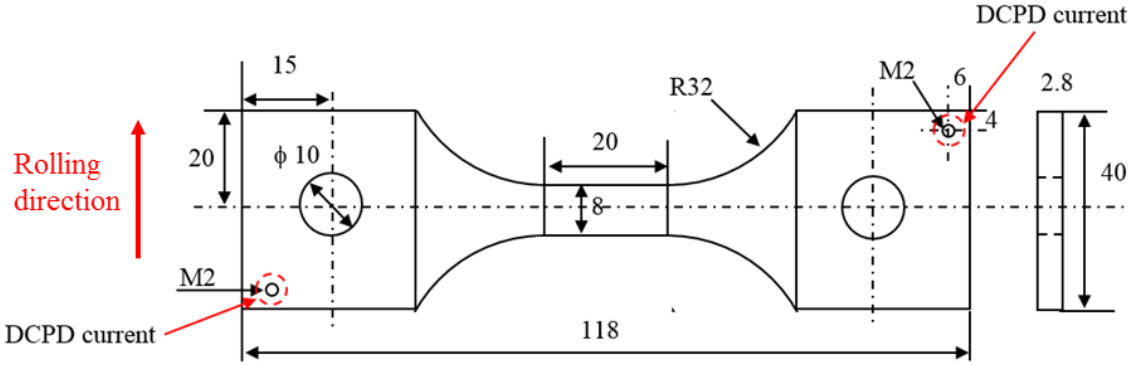

Figure 1. Schematic diagram of flat dogbone tensile specimen. All dimensions in mm ± 0.1 mm.

Table 3. Surface residual stresses of 316L SS specimens in as-received and freshly ground condition in axial and transverse direction relative to the loading direction. Standard deviation is based on 3 repeated measurements on the same location of the same specimen.

Surface finish conditions	Position from the centre of gauge length / mm	Axial Direction* / MPa		Transverse Direction** / MPa	
		Mean	STD	Mean	STD
Sequentially wet-ground to P1200	-10	-55	63	-78	49
	0	-82	51	-145	60
	10	-81	61	-195	51
As-received machined finish	0	-123	43	-23	52

*axial direction is the long transverse direction (across the width) of the rolled material **transverse direction is the rolling direction of the material.

2.2 PRE-PITTING AND PRE-CRACKING

2.2.1 Pre-pitting

A single pit with controlled depth was generated as a crack precursor by a droplet technique using a galvanostatic method established previously [4, 5]. As illustrated in Figure 2, a single droplet of 0.1 M NaCl solution was deposited at the central position of the specimen gauge section to confine the pit formation at the desired location. The droplet diameter was 2.2 mm for a volume of 2 µL and 3.0 mm for 5 µL. The specimen was anodically polarised by a galvanostatic current of 40 µA, with a 0.1 mm Pt wire placed inside the droplet as a counter electrode. The pit depth was controlled by the duration of the anodic polarisation. An example of a single pit as-produced is shown in Figure 3, with the irregular shaped pit mouth evident. The pit depth was measured by a Nikon measurement microscope. For this study, the target pit depth was in the range 100 µm to 150 µm. However, to minimize the stress level applied at the fatigue pre-cracking stage, deeper pits were introduced in some cases (e.g. specimen AFUU7). Pre-pitting parameters and pit depths are summarised in Table 4.

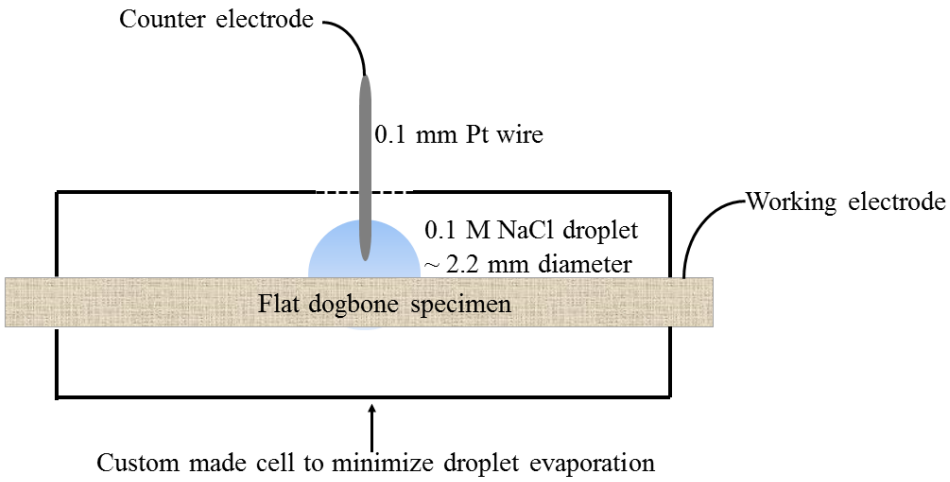

Figure 2. Schematic diagram of the droplet technique for single pit growth

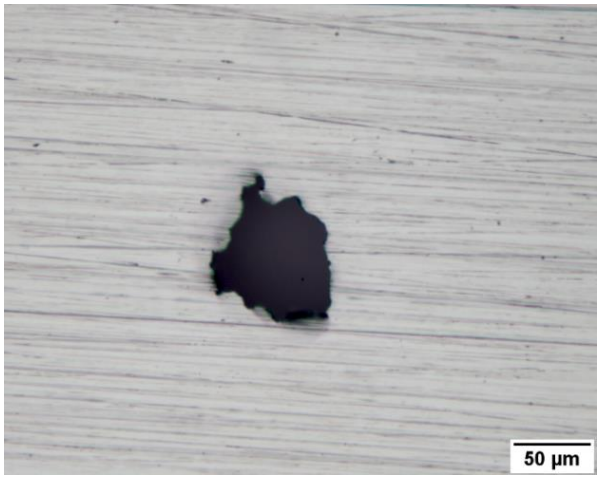

Figure 3. An example of a single pit produced using the droplet method.

Table 4. Experimental parameters for producing single pits on the 316L stainless steel specimens and as-produced pit depth.

Specimen ID	NaCl / M	Droplet volume / µL	Current / µA	Time / min	Pre-pitting depth / µm
AFUU22	0.1	2	40	30	137
AFUU15	0.1	2	40	30	130
AFUU11	0.1	5	40	30	139
AFUU7	0.1	5	40	75	205
AFUU12	0.1	2	40	25	100
AFUU9	0.1	5	40	17	108
AFUU10	0.1	5	40	40	163
AFUU5	0.1	5	40	15	90

2.2.2 Fatigue pre-cracking

Prior to SCC testing, the specimens were pre-cracked by fatigue at a stress ratio (σ_{min} / σ_{max}) of R = 0.1 and frequency = 50 Hz in air at ambient temperature. The primary reason for such pre-cracking is to provide a benchmark for the initial crack depth that would then feed into the procedure for converting potential drop into crack size. To allow exploration of the effect of the initial crack depth, pre-cracks of different surface lengths, from 280 µm to 3398 µm, were produced. During fatigue pre-cracking, the maximum applied stress (σ_{max}) was usually 95% of the nominal yield strength (i.e. 0.95 $\sigma_{0.2}$), with the exception of 0.85 $\sigma_{0.2}$ and 0.98 $\sigma_{0.2}$ for specimens AFUU7 and AFUU12 respectively. As a consequence of the relatively high stress in pre-cracking, the stress applied for the SCC testing was 1.1 $\sigma_{0.2}$, which in combination with the varying initial crack depth would give a range of initial stress intensity factors, from 4.9 MPa $m^{1/2}$ to 17.1 MPa $m^{1/2}$, as shown in Table 5. From Table 5 it can be seen that the crack depth produced for specimen AFUU5 was too large to be considered for valid growth rate measurement; hence, no data for this specimen are reported hereafter. An additional specimen was prepared that was pre-pitted but not pre-cracked (specimen AFUU22). The pit depth in that case was 137 µm (Table 4).

Table 5. Summary of pit widths (average in horizontal and perpendicular directions), pit depths and surface length of pre-cracks of the 316L SS specimens. For SCC testing the applied stress was 1.1 $\sigma_{0.2}$.

Specimens	Pre-pitting width / µm	Pre-pitting depth / µm	σ_{max} / $\sigma_{0.2}$ / %	Pre-crack surface length / µm	Initial K(SCC) / MPa $m^{1/2}$
AFUU15	123	130	95	280	4.9
AFUU11	116	139	95	393	5.8
AFUU7	99	205	85	791	8.3
AFUU12	115	100	97.5	811	8.4
AFUU9	55	108	95	985	9.2
AFUU10	106	163	95	1293	10.6
AFUU5	93	90	95	3398	17.1

2.3 IN SITU MEASUREMENT OF CRACK GROWTH RATES

2.3.1 Pulsed Direct Current Potential Drop (DCPD) system

A high resolution, multi-channel DCPD system with good long-term stability (DCM2, Matelect Ltd) was used for in situ crack growth measurements. Pt wires of 0.1 mm diameter (DCPD probes) were spot-welded on either side of the pre-pit using a microscope, with a spacing of about 0.3 mm to optimise DCPD signal resolution. The potential drop across the pit (and the crack) is denoted as V_c. Pt wires were also spot-welded to a plain surface away from the pit and crack, to provide reference potential drop measurement (V_{ref}) (Appendix 1). The ratio of V_c and V_{ref} is used for crack depth calculation to minimise the impact of potential drop variation associated with change in temperature [6].

To ensure stable attachment of the probes the welded Pt wires were created into the shape of a vertical loop. At the end of the loop, the Pt wires were encased with 0.4 mm PEEK tube, which was fixed to the substrate with a special heat-resistant epoxy resin (3M® Scotch-Weld™).

The pulsed DCPD method to measure V_c and V_{ref} was as follows. A current of 5 A was applied for 0.75 s and 64 readings of V_c and V_{ref} were taken towards the end of the pulse at an acquisition rate greater than 6.4 kHz. The application of the current was then discontinued for 0.75 s and the measurement was repeated. The average value of the difference between the readings measured with and without the applied current was then used as one data point for V_c and V_{ref} respectively. This

procedure was repeated twice to reduce the noise level of the potential readings. The whole process took approximately 3 s.

Each specimen was connected to a single DCPD channel with a pulsed current of 5 A, applied with a time period of 1.5 s as described above. Data acquisition is made for 3 s for an overall duration of 1.5 h. Therefore, for the 8 specimens tested, it took 12 h to complete one measurement cycle before starting again. During the measurement period of 1.5 h for each channel, a settling time of 0.5 h was set to allow the system to stabilise before proceeding and 1540 data points of V_c and V_{ref} were taken respectively in the next 1 h. All the acquired data were then averaged to give single values of V_c and V_{ref}.

2.3.2 Durability of DCPD probes

The durability of DCPD probes for long-term testing in a corrosive environment is always a concern. Localised corrosion of the base metal could undermine the welded contact, posing a risk of electrical connection failure, though this is more likely associated with changes in susceptibility of the spot-welded region rather than galvanic coupling, in view of the small cathodic area. To assess this risk, accelerated tests were carried out at 70 °C, 40% RH with a CDD of 264 µg/cm^2 for 1 month, during which the probe connections were checked daily. Corrosion products formed inside the salt deposition area (Figure 4, dashed circle) but the probe connections remained intact. In practice, during the test exposure period of 9 months, 60% of DCPD probes survived and the rest of the probes failed due to corrosion.

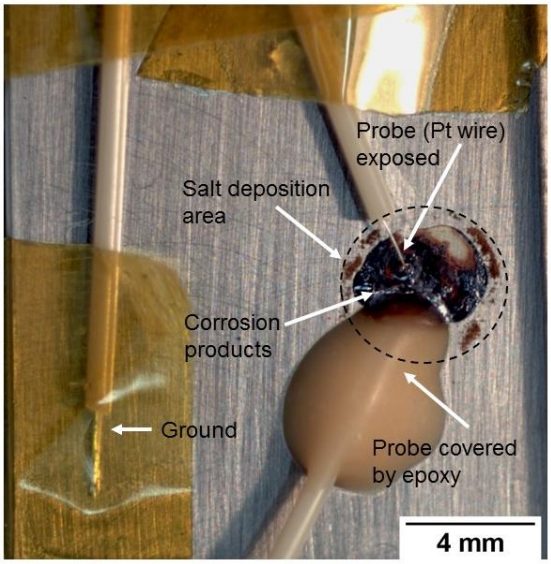

Figure 4. Durability testing of Pt probe connection for the DCPD system.

2.3.3 Evaluation of DCPD thermal heating effect

Passing a current through the specimen in atmospheric conditions (and poor thermal conductivity of the surrounding environment) could lead to a temperature increase, which would not be observed in full immersion tests. The induced thermal heating could result in uncertainty in the voltage measurement (i.e. thermally induced voltage change). The thermal heating effect was evaluated by measuring the specimen surface temperature in air at different locations (centre and edge) at an applied current of 5 A for each measurement cycle of 3 h. It is evident from Figure 5 that the temperature increase induced by the current is no more than 0.2 °C, which suggests that the thermal heating effect during the operation of the DCPD can be neglected.

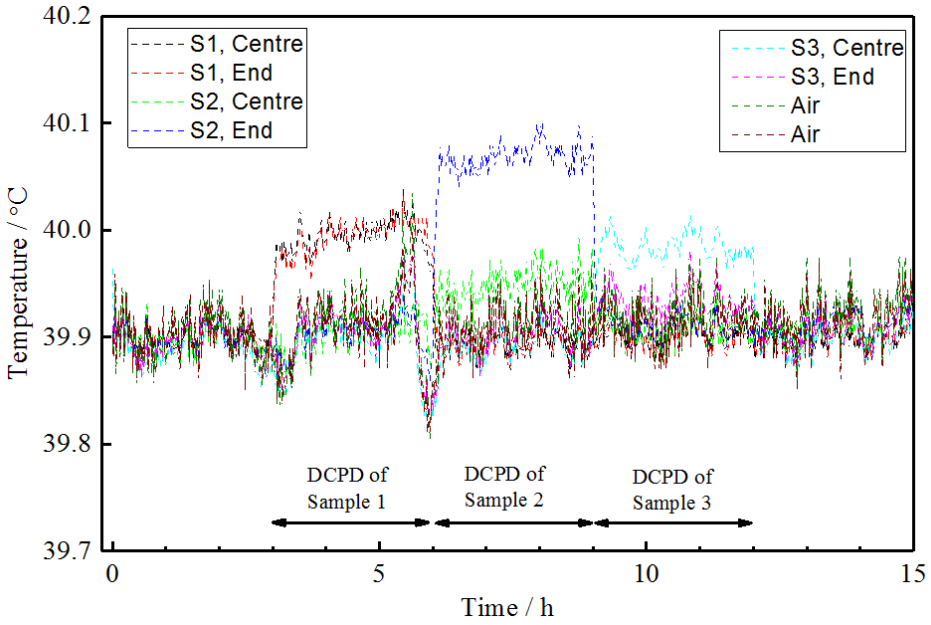

Figure 5. Thermal heating effect induced by the pulsed multichannel DCPD system.

2.3.4 Conversion of DCPD signals to crack depth

A generic analytical model was established previously [6] to correlate the measured potentials with crack depth for small cracks. Good agreement between the predicted crack depths from DCPD and experimental measurements from fracture surfaces has been shown in previous work [7]. The methodology for the present application is described in Appendix 2 to this report.

2.3.5 Measurement uncertainty of DCPD system

The intrinsic measurement uncertainty of the DCPD system was determined as follows. DCPD measurements were carried out on a dummy specimen connected to a single channel for a period of about 140 h in the testing chamber at 40 °C and 40% RH, as shown in Figure 6. The measurement uncertainty in the DCPD when converted to the apparent crack depth was about 0.01 μm. Therefore, the measurement uncertainty in crack growth rate, for instance over the 140 h period, would be 2×10^{-14} m/s (i.e. 0.01 μm/140 h). It should be noted that the uncertainty in crack growth rate varies with the measurement period and the noise level associated with each specimen.

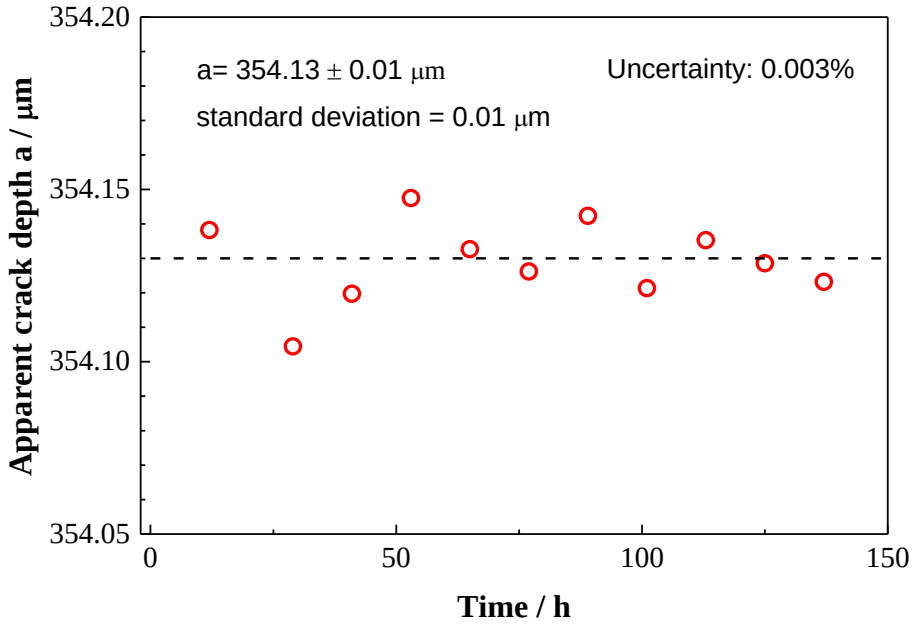

Figure 6. Measurement uncertainty in the crack depth from a single channel of the DCPD system for a test period of 140 h.

2.4 TEST PROCEDURE

For the exposure tests, specimens were loaded in a calibrated proof ring apparatus (Figure 7). An applied stress of $1.1\sigma_{0.2}$ (i.e. 361 MPa), higher than that used during fatigue pre-cracking, was selected for these measurements. The tensile force was produced by tightening the screws on the outside of the ring. Initial stress relaxation was observed at room temperature due to the creep of the material. Measurement of the displacement of the proof ring indicated that the applied stress decreased by about 3% over a 12 h period. Therefore, the relaxation was compensated by increasing the load until the stress reduction was less than 1% after 12 h prior to the testing. This protocol was applied for the loading of each specimen.

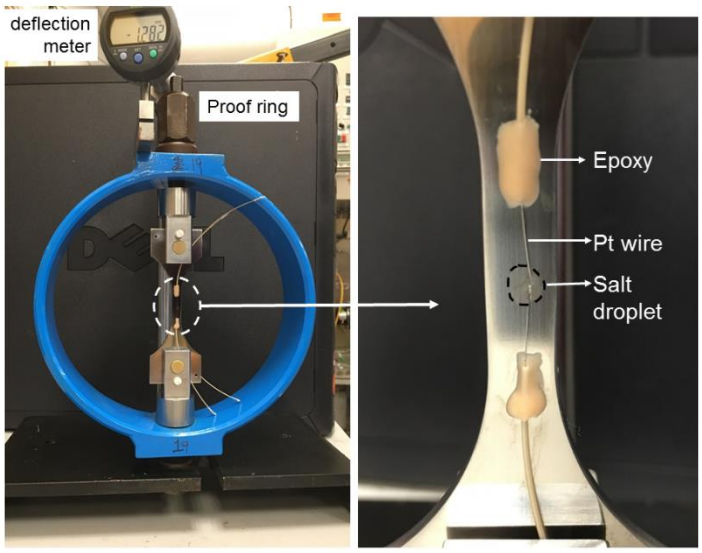

Figure 7. Proof ring set-up with loaded specimen. The detailed figure on the right shows the salt deposition area (dashed black circle) and spot-welded Pt wires for DCPD connection prior to exposure in the climate-controlled chamber.

$MgCl_2$ ($MgCl_2 \cdot 6H_2O$, Certified AR grade, Fisher Scientific) aqueous solution (diluted by deionised water, 18.2 MΩ-cm) was prepared for the droplet deposition at the centre gauge section of the specimen. It can be seen from Figure 7 that the droplet area covers the pre-pit, the pre-crack and the spot-welded Pt probes for DCPD connections. 22 mM $MgCl_2$ solution was chosen to give an approximate CDD of 100 µg/cm^2 for a 7 µL droplet covering an area of ~ 11.1 mm^2. It should be noted that the presence of the Pt wires and/or possible surface contaminants perturbed the droplet shape on deposition, which could give some uncertainty in the CDD and possibly heterogeneous distribution of chlorides on surface. The droplet area for each specimen was measured again after evaporation to confirm the target CDD values. Broad consistency in CDD was achieved (average of 105 µg/cm^2), with the exception of specimen AFUU12, for which the CDD was 47 µg/cm^2.

The proof ring containing the salt-loaded specimen was then placed in a climate-controlled chamber (ESPEC® ARL-0680, Japan), as shown in Figure 8. The temperature was maintained at 40 °C. The defined humidity conditions were as follows: 40% relative humidity (RH) for a total period of 2300 h; the RH was then increased to 60% for a period of 1650 h; the RH was then further increased to 80% for an exposure period of about 1430 h; finally, the RH was decreased to 60% RH for about 1120 h. The total test duration was about 9 months. All changes in RH conditions were ramp-controlled at 5% / h. In general, values of the RH and changes between different regimes were designed to test the effect of the variability of conditions within the HAW stores.

A calibrated hygrometer (Rotronic HydroClip HC2A-S, UK) was placed inside the climatic chamber to measure the temperature and humidity. All RH and temperature values cited in this report are based on readings from the calibrated hygrometer.

Figure 8. The climate-controlled chamber for atmospheric-induced SCC testing.

2.5 MEASUREMENT OF STRESS RELAXATION POST-TEST

Some relaxation of the stresses on the test specimen is expected for a test of 9 month duration despite compensation in the test procedure for short term relaxation (see 2.4). The extent of that relaxation was measured for each specimen at test termination and is shown in Figure 9. Relaxation was apparent in all specimens with the average relaxation about 14%. Specimen AFUU22 had the highest stress relaxation, 23%, whilst specimen AFUU15 had the lowest stress relaxation, 5%. For small cracks, the crack wall displacement would be small. Indeed there was no correlation of the relaxation with crack size, indicating the predominant impact of long-term creep.

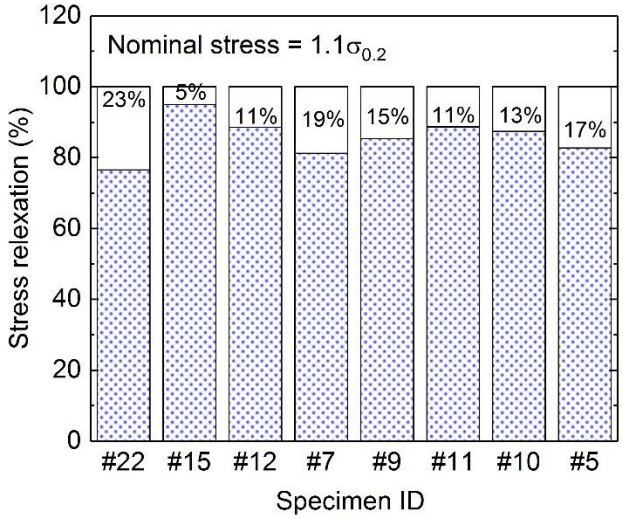

Figure 9. Stress relaxation of each specimen (ID number as shown above) at the end of test exposure after 9 months.

2.6 POST-TEST ANALYSIS

On completion of SCC testing, the loosely adherent corrosion products were removed by lightly abrading the surface. Optical images were taken and the specimens then fatigue-fractured in air at stress levels ranging from 90% to 95% $\sigma_{0.2}$ (R=0.1, *f*=30 Hz). The fractured specimens were ultrasonically cleaned in deionised water, methanol and acetone. No chemical cleaning of the surface was carried out at this stage. The specimens were examined initially with 3D confocal microscopy (Alicona G5 optical microscope) to provide an estimate of final SCC crack depth and surface length. To allow more detailed analysis of the fatigue pre-crack and SCC extension, surface oxides were subsequently removed by chemical cleaning of the specimens using Super Clarke's solution (5 g/l of 1,3-Di-n-butyl-2-thiourea in 18.8% HCl) in an ultrasonic bath for 5 min. The specimens were then examined under scanning electron microscopy (SEM, Zeiss Supra 40) with an electron energy of 10 kV and a 60 µm aperture. Measurement of initial and final crack depths, surface lengths and crack aspect ratio, a/c, obtained from both 3D confocal microscopy and SEM, were used to provide calibration data in converting potential drop measurement to crack size.

For the specimen with no pre-existing crack (AFUU22), the dimensions of the pit acting as the stress corrosion crack precursor were measured.

2.7 METHOD OF ESTIMATING CRACK GROWTH RATES

Crack growth rates were estimated based on the well-defined incremental polynomial method applied to the crack depth vs time data, as described in BS ISO 12108:2012 [8]. The crack growth rate was calculated at 30-50 µm increments in depth, fitting with a polynomial to the data for each increment, if the growth rate was relatively fast (i.e. more than 1×10^{-11} m/s). When the growth rate was slow (i.e. less than 1×10^{-12} m/s) and the overall crack advance was small, the approach was to choose a smaller increment, typically 10 µm, and adopt a linear fit over that crack-size range.

3 RESULTS

3.1 TEST CONDITIONS

Figure 10 shows an overview of the RH and temperature conditions during the SCC testing. The temperature was maintained nominally constant at 40 °C, although a small monotonic decrease in temperature of about 0.2 °C was apparent over the 9 month exposure period. During the initial RH exposure at 40%, there is some variability in the RH, which was due to short transients of instability of the chamber. More significantly, an uncontrolled RH disturbance occurred between 1445 h and 1704 h, during which the RH decrease to values as low as 5% due to malfunction of the humidity control probe. This incident impacted on the crack growth behaviour of the specimens, which will be discussed in more detail in Section 3.3.

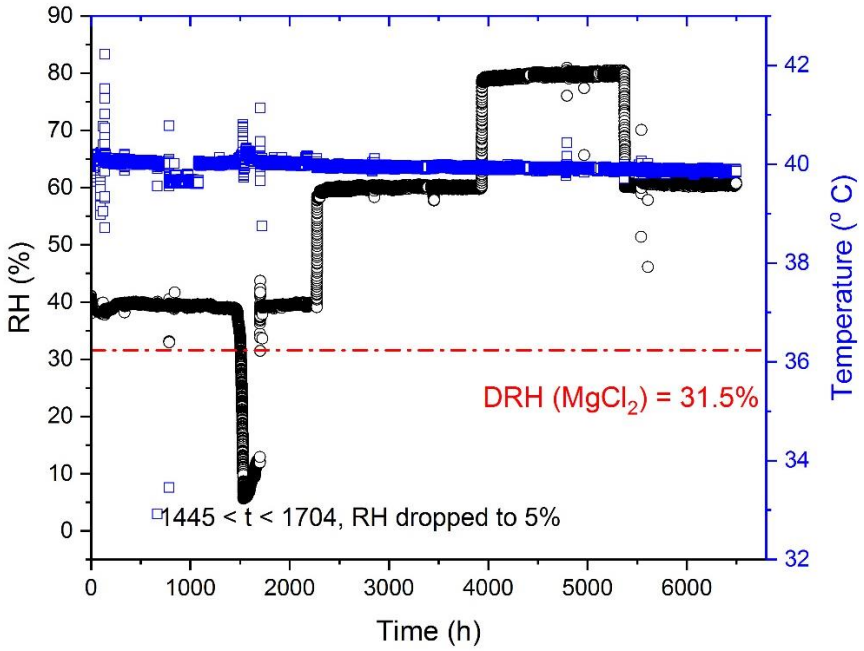

Figure 10. Time variation of RH and temperature during SCC testing of the 316L SS specimens. The Deliquescence Relative Humidity (DRH) of $MgCl_2$ at 40 °C is also indicated in red (31.5%).

3.2 FRACTOGRAPHY AND SCC PROPAGATION

Fractographic analysis of all specimens at the end of testing was conducted to reveal the existence and extent of SCC propagation for each specimen. To provide a basis for analysis and interpretation of the observations, a summary of each specimen history is illustrated schematically in Figure 11. Failure of the spot-welds occurred for specimens AFUU11 and AFUU10. Removal of the specimen and spot-welding again caused so much perturbation of the droplet and local chemistry that no useful data could be obtained afterwards. Satisfactory DCPD data were obtained for two specimens (AFUU15, AFUU22) but, for these specimens, the SCC initiated and propagated from new pits produced by atmospheric corrosion, instead of the crack precursor (i.e. pre-crack and/or pre-pit). Reliable DCPD measurements were obtained also for specimens AFUU7, AFUU12 and AFUU9 (in order of increasing pre-crack size) that had been pre-pitted and pre-cracked. The initial and final crack depth, as well as crack aspect ratio a/c, were measured from fractography and are summarised for the two groups of specimens in each section below.

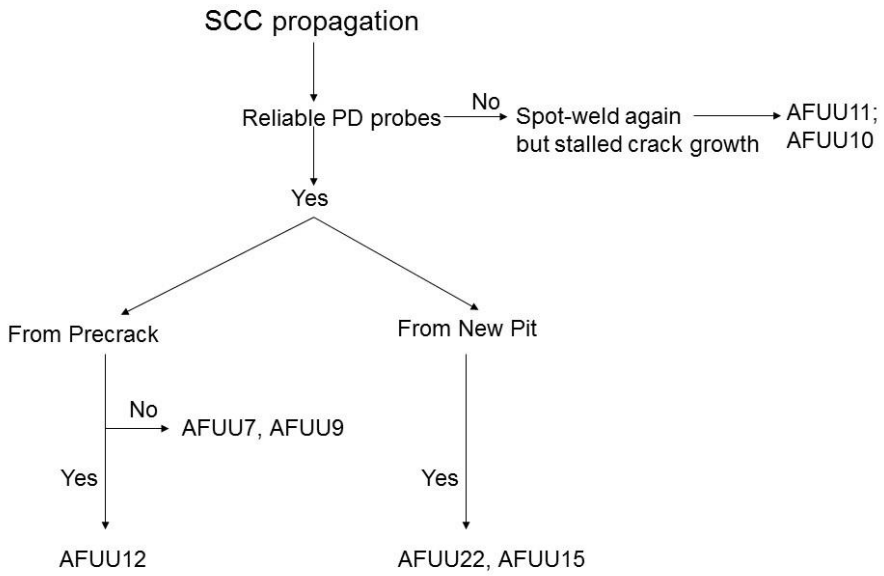

Figure 11. Overview of SCC propagation of all valid specimens. Specimen AFUU5 was excluded from the analysis as the pre-crack size was too large to consider.

3.2.1 Specimens AFUU7, AFUU12, AFUU9 (pre-pitted and pre-cracked)

The SEM fractography for each of these specimens is shown in Figure 12-15, with the notation of final crack depth a_f, final crack surface length $2c_f$, final crack aspect ratio a_f/c_f on each image. No crack extension due to SCC could be discerned in specimens AFUU7 (Figure 12) and AFUU9 (Figure 15). However, for AFUU12, a clear SCC extension from the pre-crack was observed (Figure 13), characterised by fissures oriented parallel to the stress axis (Figure 13) and a non-uniform crack front (Figure 14). Assigning a and c values for such a crack front to input into the analytical model for converting potential drop to crack depth is a clear challenge. The implications for estimating crack growth rate are discussed later.

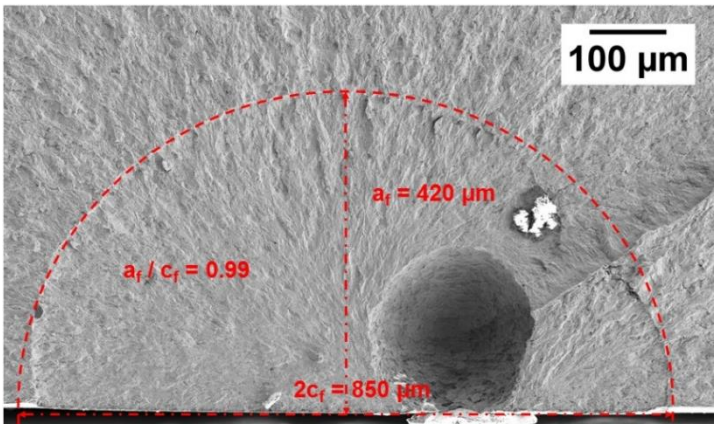

Figure 12. SEM fractograph of AFUU7 (i.e. cross section), including pre-pitted and fatigue pre-cracked area; a_f is the final crack depth, $2c_f$ is the final crack surface length, a_f/c_f the final crack aspect ratio. Note that the direction of the applied stresses in the figure was perpendicular to the page. No SCC propagation was observed on this specimen (the highlighted dashed line is associated with the fatigue pre-crack area).

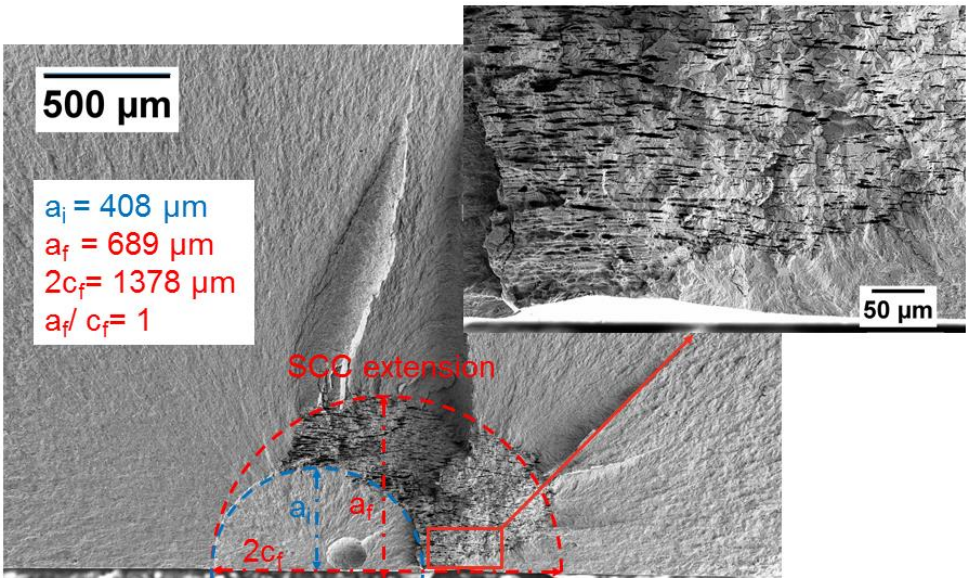

Figure 13. SEM fractograph of AFUU12 (i.e. cross section). The detailed view characterises the lateral fissures observed in the SCC region, as noted in the dashed red line. The pre-pit and pre-crack are also noted by the dashed blue line, to distinguish from the SCC area. a_i is the initial crack depth, a_f is the final crack depth, $2c_f$ is the final crack surface length, and a_f/c_f the final crack aspect ratio.

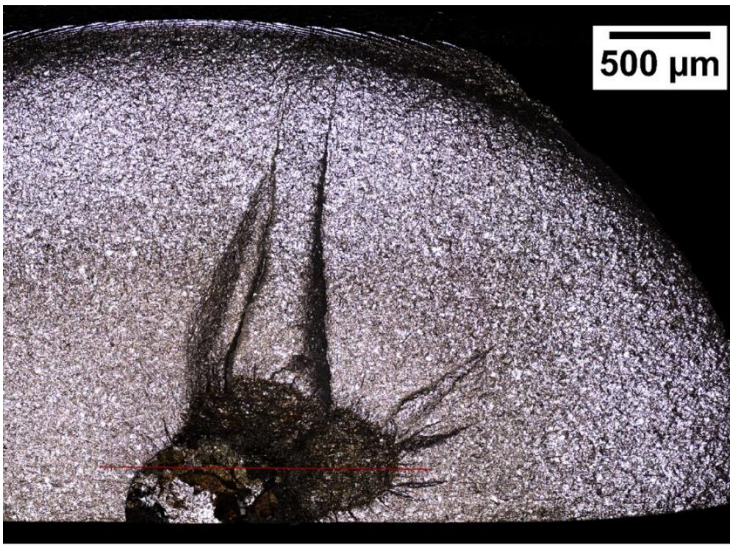

Figure 14. 3D confocal microscopy of the fracture surface of AFUU12.

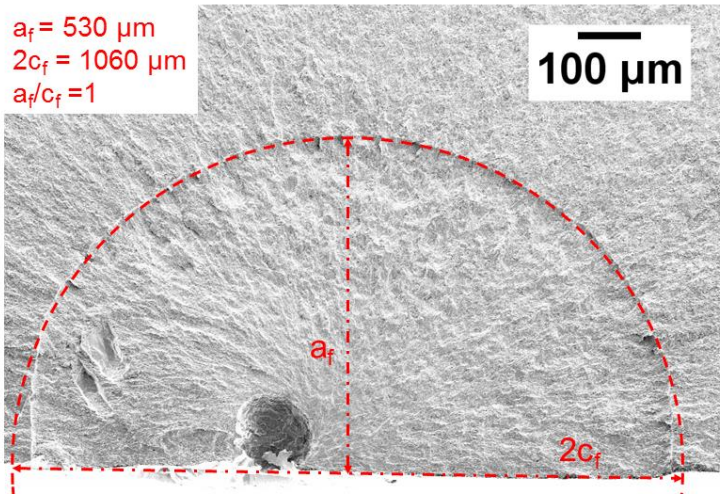

Figure 15. SEM fractograph of AFUU9 (i.e. cross section), including pre-pitted and fatigue pre-cracked area; a_f is the final crack depth, $2c_f$ is the final crack surface length, a_f/c_f the final crack aspect ratio. Note that no SCC propagation was observed in this specimen; the highlighted dashed line is associated with the fatigue pre-crack area.

3.2.2 Specimens AFUU22, AFUU15 (stress corrosion cracks developing from new pits formed during exposure)

The external surface of the pre-pitted (but not pre-cracked) specimen AFUU22 is shown in Figure 16. New pits formed close to the DCPD probe, which then led to SCC propagation and subsequent crack growth underneath the probe electrical connection (which nevertheless remained intact). Similarly, for specimen AFUU15 (pre-pitted and pre-cracked), a new pit was formed close to the DCPD probe (Figure 17), which then led to crack initiation and propagation underneath the probe (which also remained intact). The new pits produced had a depth less than 100 µm, and a geometry factor (pit depth / ½ pit width) >1 (Figure 18 and Figure 20).

The extent of stress corrosion crack propagation from the new pits for specimens AFUU22 and AFUU15 was much more substantial compared with that for specimen AFUU12 (Figure 18-Figure 21). For specimen AFUU15, the stress corrosion crack was approximately semi-circular in shape but for specimen AFUU22 the shape was more semi-elliptical. In both cases, the stress corrosion cracking was characterised by horizontal fissures (Figure 22), similarly to that seen for AFUU12.

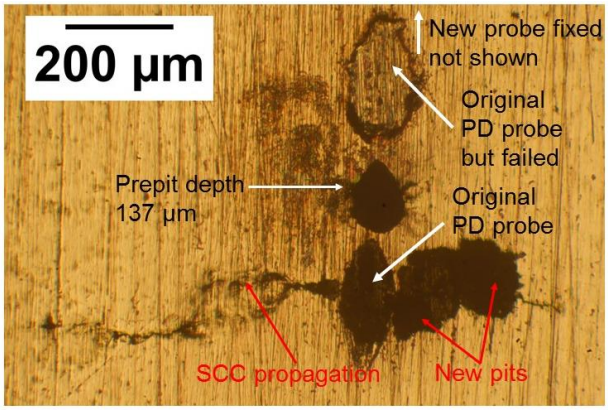

Figure 16. Formation of new pits and SCC propagation close to the DCPD probe (or PD probe noted in the figure) on AFUU22. Location of two original probes are indicated. One of the original DCPD probes with pit formation and crack transition remained intact; the other probe failed and was replaced by a new probe, attached just outside the field of view of this image.

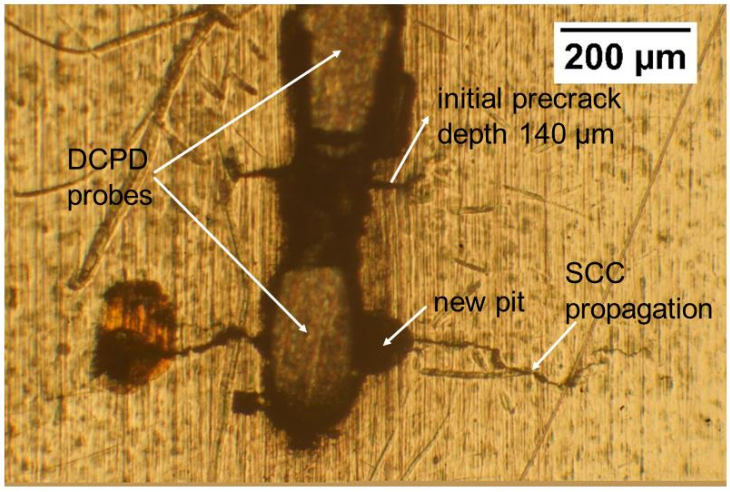

Figure 17. Formation of a new pit and SCC propagation close to the DCPD probe on AFUU15. Location of DCPD probes is indicated.

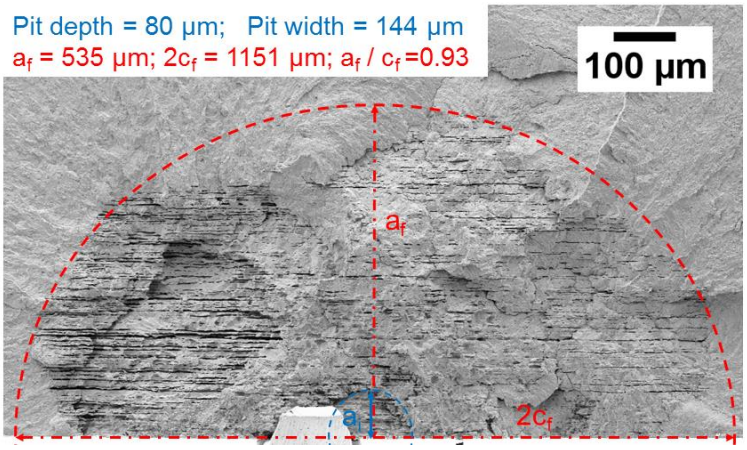

Figure 18. SEM fractograph of AFUU15 (i.e. cross section). The formation of new pit is indicated by the blue dotted line; the SCC area is indicated by the red dotted line; a_i is the initial crack depth, a_f is the final crack depth, $2c_f$ is the final crack surface length, a_f/c_f the final crack aspect ratio.

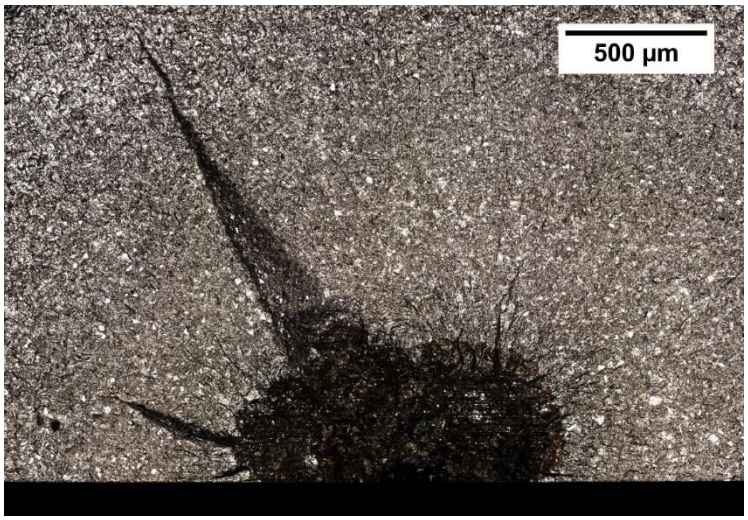

Figure 19. 3D confocal microscopy of the fracture surface of AFUU15.

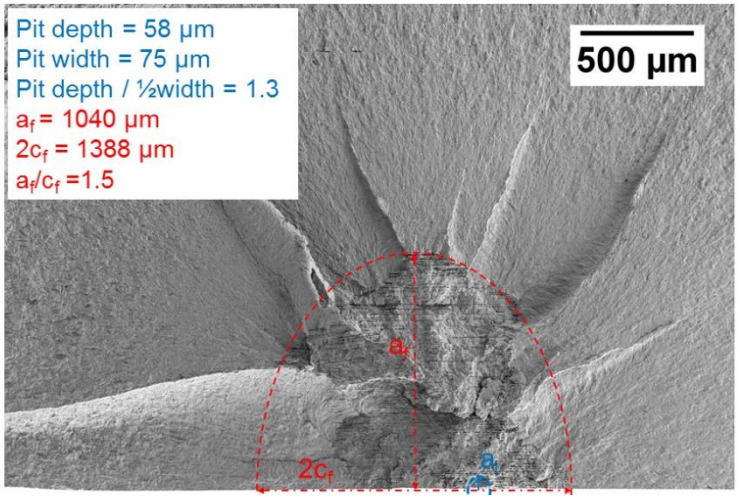

Figure 20. SEM fractograph of AFUU22 (i.e. cross section). The formation of new pit is indicated by the blue dotted line; the SCC area is indicated by the red dotted line; a_i is the initial crack depth, a_f is the final crack depth, $2c_f$ is the final crack surface length, a_f/c_f the final crack aspect ratio.

Figure 21. 3D confocal microscopy of the fracture surface of AFUU22.

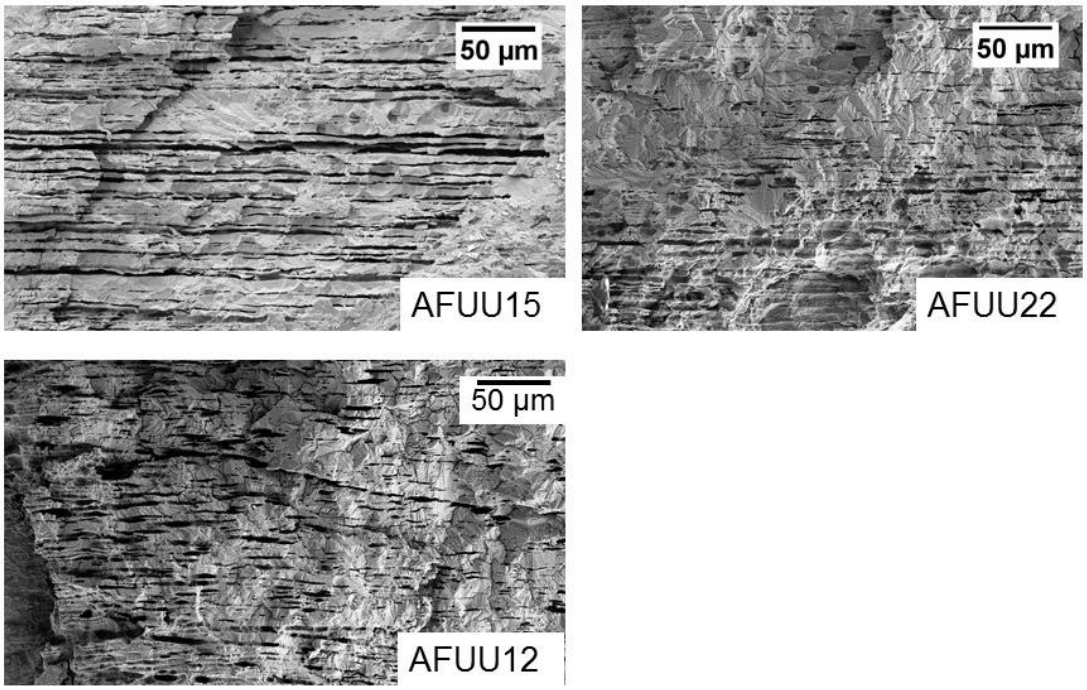

Figure 22. Horizontal fissures (in parallel with stress axis) in SCC region of AFUU15, AFUU22 and AFUU12.

Table 6 summarises the initial pit depth and final crack depth, as well as their geometry factors (depth / ½ surface length), of AFUU22 and AFUU15.

Table 6. New pit depth (µm) and final crack depth (µm) and crack aspect ratio of AFUU22 and AFUU15.

Specimen ID	New pit depth	a_i / c_i	Final crack depth	a_f / c_f
AFUU22	58	1.3	1040	1.50
AFUU15	80	1.1	535	0.93

3.3 CONVERTING POTENTIAL DROP TO CRACK SIZE AND HENCE TO CRACK GROWTH RATE

The in situ DCPD measurements were converted to stress corrosion crack depth by the analytical model detailed in Appendix 2.

3.3.1 Potential drop drift

The measurement uncertainty of the DCPD system on a plain surface dummy specimen at 40 °C and 40% RH was shown in Figure 6. The noise associated with the potential drop signal for a measurement period of 140 h was found to be 0.03 µV. Thus, the DCPD system used in these measurements is

nominally a very stable measuring tool. However, in the presence of a concentrated salt droplet, the mass loss between the probes, associated with atmospheric corrosion, can lead to an increased potential drop that is not associated with the cracking process being monitored. For example, with specimens AFUU7 and AFUU9, a slight increase of about 2-3 μV in the potential drop (V_{crack}) was observed (Figure A1 and Figure A3 in Appendix 1), without discernible evidence of any crack propagation on the fracture surface. This is likely linked to corrosion attack around the edges of the DCPD probes, as well as corrosion associated with the crack-mouth opening (Figure 23). Thus, the observation of a small increase in potential drop does not in itself imply that cracking has initiated. Further supportive evidence is required.

There is no effective way of decoupling the two contributions to elicit the sole contribution due to cracking processes. Nevertheless, the potential drop data for those two tests in the absence of crack propagation suggest that the magnitude of the increase in potential drop associated with non-cracking processes is small and becomes relatively insignificant at long times, reflecting the usual trend of corrosion rates decreasing with time.

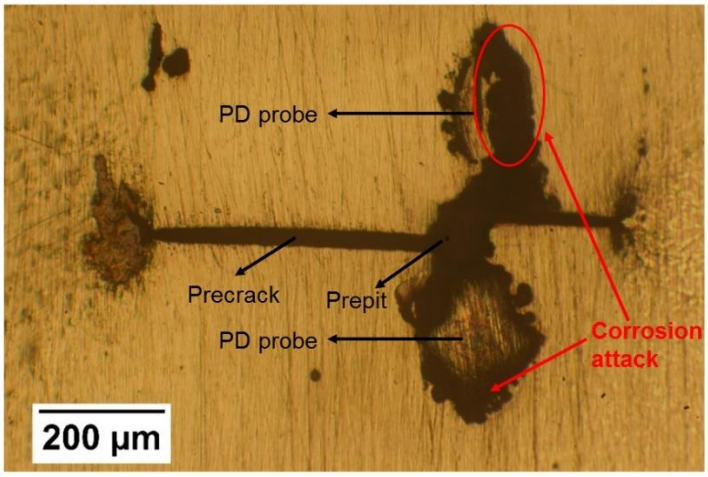

Figure 23. Evidence of corrosion attack around DCPD probes which is associated with the potential drop increase for specimen AFUU7.

3.3.2 Specimens AFUU7, AFUU12, AFUU9 (pre-pitted and pre-cracked)

In this group of specimens, the fractography indicated that only one test specimen, AFUU12, exhibited stress corrosion crack growth (Figure 13). Hence only data from that test are meaningful to analyse. It is observed that the crack shape associated with SCC from the pre-crack in specimen AFUU12 is not well-defined, unlike the cases for the other two specimens AFUU22 and AFUU15 with stress corrosion cracks from the pits. Assuming a semi-elliptical crack, the 'best fit' to the crack profile of specimen AFUU12 was assessed with a/c values ranging from 0.89 to 1.06. Values outside this range were clearly inconsistent with the crack profile. Given the relatively tight range, a value of a/c=1 was adopted (Figure 13). In converting the potential drop values in Figure A2 to crack size, the procedure outlined in Appendix 2 was adopted, with an a/c ratio of 1 assumed for the initial pre-crack and for the final crack, despite the irregularity of the crack front for the latter.

The crack depth variation with time is shown in Figure 24. Notwithstanding the uncertainties associated with the method previously discussed (i.e. changes in potential drop in the absence of cracking), the data suggest that, on average, SCC propagation rates decreased when the RH was increased from 40% to 60%, and further to 80%, and increased again when the RH was decreased back to 60%. It should also be noted that during the period of 40% RH, from 1700 h to 2000 h, there is an order of magnitude increase in the growth rate (Figure 25) following restoration of the 40% RH after the uncontrolled excursion in RH to 5%. Hence, it is unquestionable that this significant crack

growth was triggered by the period of relative drying, i.e. when RH was decreased to 5%, and subsequent rewetting upon restoration of the nominal 40%.

Prior to this excursion, the increase in potential drop (ΔV_{crack}) was about 5 µV (Figure A2). It is possible that this increase of 5 µV is not related to crack extension but to material loss from corrosion, as observed with specimens AFUU7 and AFUU9, but it is not possible to be definitive. The stress corrosion crack development after the excursion appeared to be kick-started by the drying and re-wetting process in this particular specimen (although not in AFUU7 or AFUU9). However, there is no way of determining this from the fracture surface and hence, as a default, it is necessary to assume that the potential drop change in this region could be associated with crack extension.

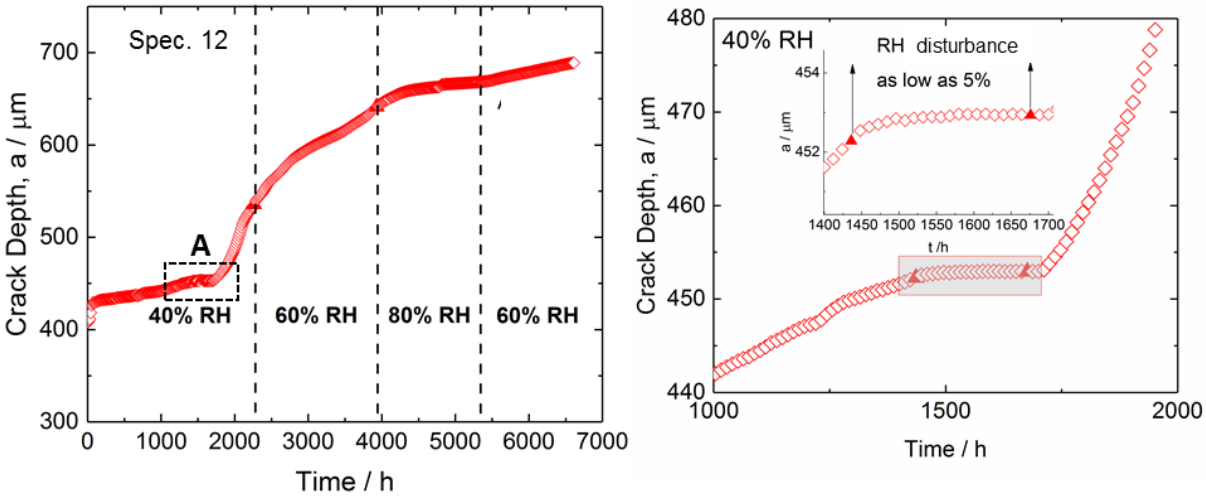

Figure 24. In situ crack growth of specimen AFUU12 as a function of time during different RH regimes. Highlighted region A in the left figure (in which the RH accidently dropped to ~ 5%) is shown in detail on the right.

The crack growth rates calculated from Figure 24 at different crack depths are plotted in Figure 25. In this and subsequent similar figures the crack growth rate data are shown at discrete depths only, for presentational purposes. With the assumption noted above (i.e. the increase in potential drop prior to the RH excursion is associated with crack growth), an initial crack growth rate of 3×10^{-12} m/s is estimated. Following the excursion, the crack growth rate increased markedly, reaching a maximum of 5×10^{-11} m/s, although slowing down slightly with increased crack depth. With increase in RH to 60%, the growth rate decreased progressively with crack depth to about 1×10^{-11} m/s at the termination of this RH exposure period. Upon increasing the RH to 80%, the crack growth rate decreased further, towards 1×10^{-12} m/s (i.e. 32 µm/year). Considering a component thickness of 3 mm, 10^{-12} m/s is about the threshold of crack propagation rate to give a 100 years of component life. Finally, when the RH of 80% was reduced to 60%, to assess whether reactivation of the higher crack growth rate would occur, the crack growth rate increased to about 4×10^{-12} m/s, indicating a degree of reactivation.

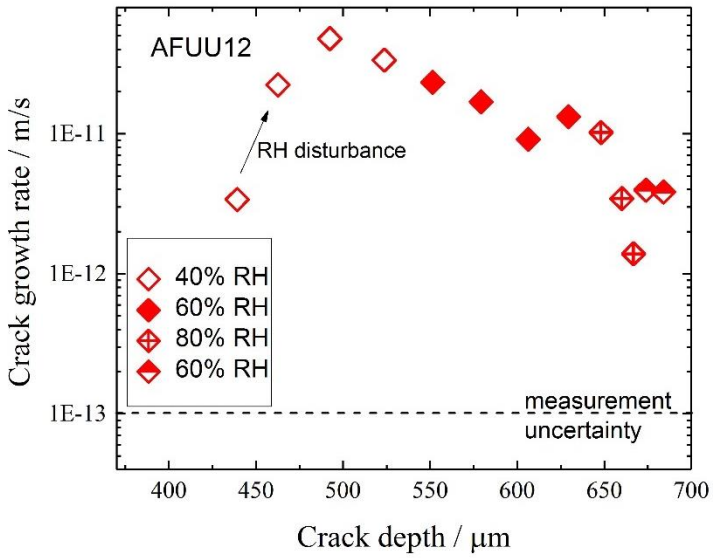

Figure 25. Crack growth rates as a function of RH for AFUU12 at distinct crack depths. The RH disturbance is noted to highlight its step-wise effect on the increased growth rate.

3.3.3 Specimens AFUU22, AFUU15 (stress corrosion cracks developing from new pits formed during exposure)

In the tests involving specimens AFUU22 (Figure 18) and AFUU15 (Figure 20) the crack evolved from pits developed during the test rather than from pits or cracks formed prior to the tests. This poses a challenge in several ways:

- the evolving pit contributes to the potential drop in the early stages;
- the pit depth at which the pit-to-crack transition occurred is uncertain;
- the assumed crack shape upon initiation can only be approximated.

For these specimens, the approach adopted was to assign an arbitrary semi-elliptical crack-like defect with small size present at time zero, and to associate this with the first potential drop measurement. For the current investigation of specimen 15 and 22, the initial defect sizes were assumed to be 5-10 μm. As outlined in Appendix 2, an initial estimate of the crack depth evolution with time is then projected. The predicted value of the final crack depth is then compared with the measured value until the agreement of the two is reached by reasonable adjusting of the probe spacing L_p. The limitation of this approach is that the growth of the pit and the associated change in potential is not account for explicitly, the voltage has been assigned to a crack at all times. This potentially leads to an overestimated crack growth rate at early stages, due to the three dimensional nature of the pit, and the greater resistance developed associated with material loss. The impact of the initial crack size assumption on the crack depth evolution was assessed and is shown in Figure B2. For the assumption of different initial crack depth, the uncertainty is found mostly at the early stages with crack depth less than 60 μm. In other words, the projected values become independent of the assumed initial crack depth for crack depths in excess of 100 μm.

For specimen AFUU15 the aspect ratio of the pit and the final crack shape was similar, i.e. a/c close 1, which removed a source of uncertainty in the analytical conversion of potential drop to crack depth. For specimen AFUU22, the pit shape and crack shape were a little different with a/c of 1.3 for the pit and 1.5 for the crack. As an approximation, a single value of 1.5 was adopted for initial effective crack size and final crack size. The impact of that approximation on crack size and crack growth rate is unlikely to be very significant and then only relatively important when the crack depth is small.

The time dependence of the crack depth is shown in Figure 26 and the depth dependence of the crack growth rate in Figure 27. Initially, at 40% RH, the crack growth rates for the two specimens were quite similar, at about 3×10^{-11} m/s. After 1000 h, specimen AFUU15 maintained a moderately fast growth rate (from 3×10^{-11} m/s up to 1×10^{-10} m/s). The uncontrolled RH excursion (RH down to ~5%) caused the crack propagation to arrest for specimen AFUU15 but the crack growth rate recovered to the previous rate with restoration of the normal RH condition (Figure 26, part B). The crack growth rate was of the order of 9×10^{-11} m/s before and after the RH transient. In contrast, the drop in RH significantly impacted the growth rate of specimen AFUU22, resulting in a higher crack propagation rate after the RH was recovered than before the transient, somewhat similar to the enhancement observed for AFUU12. In particular, the growth was accelerated by almost one order of magnitude after the uncontrolled RH disturbance, reaching a maximum of about 1×10^{-10} m/s, similar to the rate observed for specimen AFUU15. This crack growth rate of specimen 22 was sustained during the rest of the exposure period at 40%.

Following the increase in RH from 40% to 60%, the crack growth rate of both specimens showed clear signs of slowing down with increasing crack depth. For specimen AFUU15, the crack propagation rate decreased to about 1×10^{-11} m/s. For specimen AFUU22, the relatively high crack growth rate measured at 40% RH (1×10^{-10} m/s) was sustained initially but then decreased gradually to 3×10^{-11} m/s by the end of the exposure at 60% RH.

At 80% RH, both specimens demonstrated a gradual decrease in growth rate as a function of time (or increased crack depth). For specimen AFUU15, the growth rate was initially about 1×10^{-11} m/s but then dropped below 1×10^{-12} m/s at the later stage of the 80% RH exposure. For specimen AFUU22, the growth rate decreased from 3×10^{-11} m/s to 1×10^{-12} m/s soon after the increase in RH. Hence, by the end of exposure period of 80% RH, both specimens AFUU15 and AFUU22 specimens showed similar growth rates at 1×10^{-12} m/s.

During the final 60% RH period, the crack growth rates of both specimens increased. From Figure 27 it can be observed that when the RH was varied from 80% to 60%, both specimens showed an increased growth rate from about 1×10^{-12} m/s to about 3-5 $\times 10^{-12}$ m/s. With continued exposure for up to 1000 h, the growth rates of both specimens indicated some signs of slowing down, but not too significant.

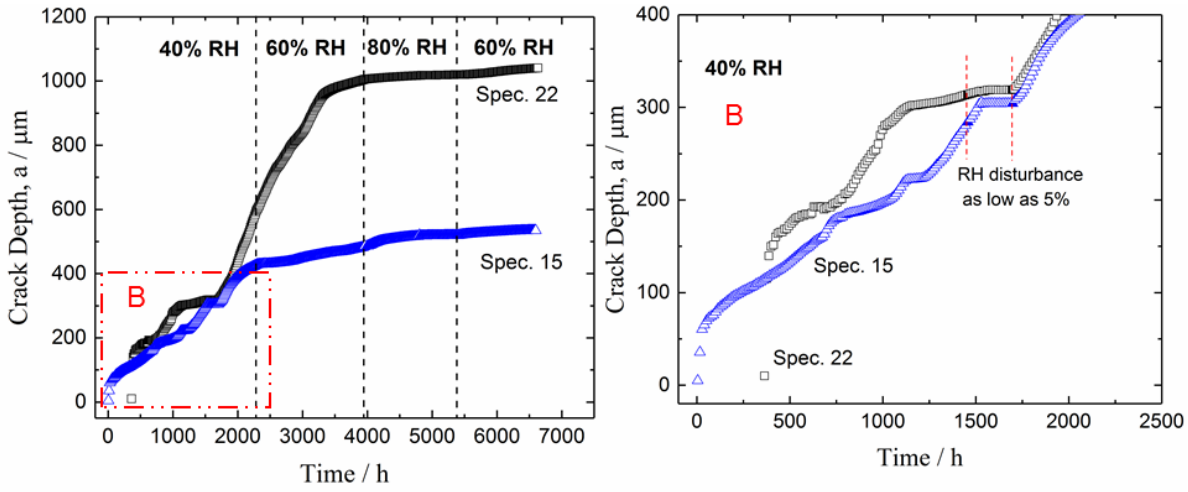

Figure 26. In situ crack growth of AFUU15 and AFUU22 as a function of RH. The absence of data for time before about 360 h in specimen AFUU22 was a consequence of probe connection failure in the early stages of testing (Figure 16). The specimen was removed from the chamber for new probe attachment prior to the following exposure. Note the initial crack sizes for specimen AFUU15 and AFUU22 were assumed to be 5 µm and 10 µm respectively.

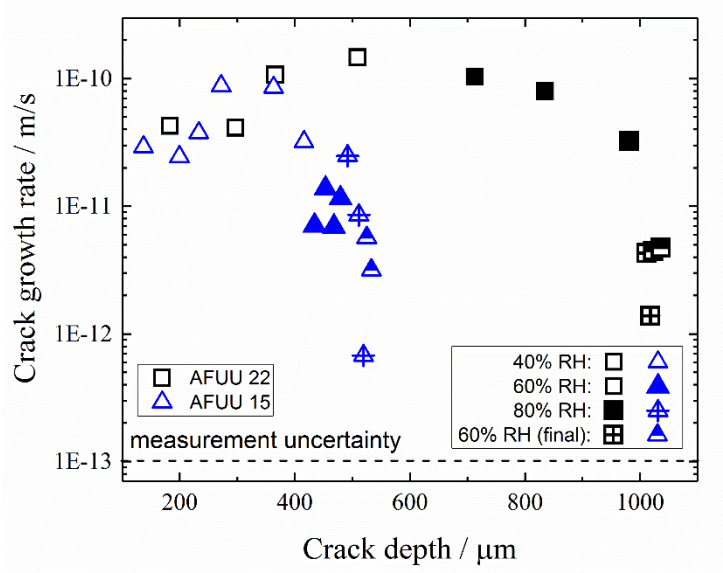

Figure 27. Crack growth rates as a function of RH at distinct crack depths for specimens AFUU15 and AFUU22.

4 DISCUSSION

4.1 METHODOLOGY AND MORPHOLOGY OF ATTACK

The unexpected feature of this set of tests was the relative ineffectiveness of pre-pitting and fatigue pre-cracking in acting as a precursor to initiation of stress corrosion cracking, despite the success of this methodology in other applications [7]. Since the fatigue crack and stress corrosion cracks were both transgranular, this is not an issue of transitioning of the crack mode. Stress corrosion crack growth was observed for one test with a pre-crack, specimen AFUU12, despite having the lowest CDD, 49 µg/cm^2 compared to the target value of 100 µg/cm^2, but apparently only in response to a temporary excursion in RH to a dried-out state. However, new pits formed during exposure readily transformed to stress corrosion cracks. One explanation for the latter is the role of dynamic plastic strain induced by a pit growing in a strain field at high stress, in facilitating the pit to crack transition, which would prevail only for growing pits [9]. While this may contribute to the phenomenology observed, new pits and stress corrosion cracks were characterised also by significant attack on the microstructure, reflected in the formation of fissures parallel to the stress axis. The height of horizontal fissures was found to be about a few microns with a spacing of about 10 µm. The fissures may reflect the preferential dissolution of a susceptible phase and are best correlated to the residual delta ferrite band formed along the rolling direction, as shown in Figure 28. Preferential dissolution of ferrite in austenitic stainless steel was reported previously, associated with pitting in 304L SS [10].

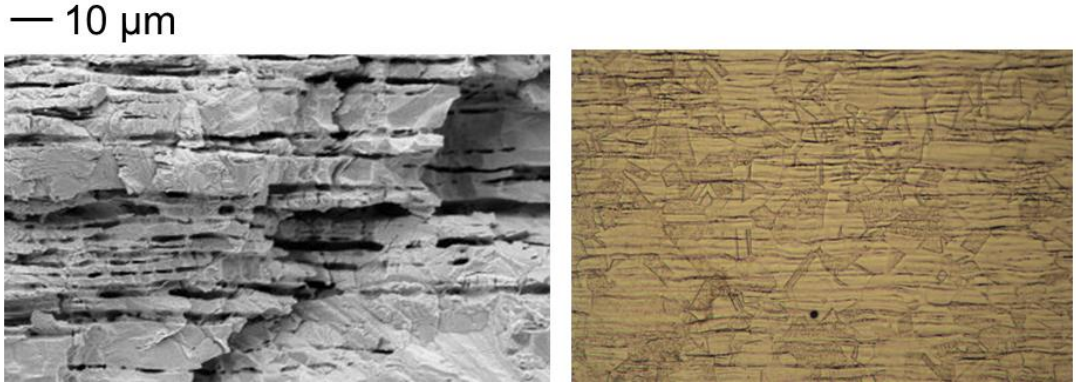

Figure 28. SEM image of ferrite attack on SCC of specimen AFUU15 (left) and etched microstructure (right) on the cross-sectional area of 316L SS dogbone specimens. The rolling direction is horizontal to the figure (i.e. across the page).

It can be suggested also that the chemistry inside the active pits and evolved stress corrosion cracks was much more aggressive than in the pre-cracks. However, this invites the question as to why there is such a sharp transition in this microstructural attack in progressing from a pre-crack to a stress corrosion crack for specimen AFUU12 (e.g. Figure 13). Could the chemistry really change that abruptly? Retained air in the pre-crack (hindering parts of the pre-cracked area from exposure to aqueous conditions and subsequent corrosion) is not compatible with the extent of oxide product observed on the fracture surface in the pre-crack region (except perhaps in very small local regions) and does not provide an explanation. Accepting that the chemistry is evidently more aggressive in the new pits and stress corrosion cracks, one possibility for the apparently abrupt transition is that the pre-pit and pre-crack region act as net cathodes, constraining attack of the microstructure. Local dynamic plastic strain in combination with an aggressive environment leading to attack of the microstructure could also be invoked, but since such microstructural attack has been observed in atmospheric pits with no applied stress [10], a purely chemical/electrochemical explanation seems more tenable. However, why then did attack on the microstructure not proceed when pre-pitting in the present investigation? The latter was conducted in a solution of 0.1 M NaCl at a small applied galvanostatic current of 40 μA. This was sufficient to drive the pitting but the local environment was apparently not aggressive enough to attack the ferrite. The pitting study [10] in which ferrite attack was reported involved a test solution of saturated $MgCl_2$ under atmospheric corrosion conditions. It seems likely that a higher chloride concentration was developed in the pit compared to that developed using the galvanostatic method.

It is also necessary to explain why the effective drying out, as a consequence of the uncontrolled drop in RH to 5%, should have led to accelerated stress corrosion crack growth of AFUU12 (and possibly AFUU22) on rewetting. Indeed, in relation to the AFUU12, it may have been the trigger to initiate stress corrosion cracking. On restoration of the RH to 40%, there would be a transient increase in $[Cl^-]$ to saturation level, ~12 mol/kg H_2O, at the deliquescence point for $MgCl_2$ of 31.5%. In addition, the drying and wetting process of the salt could lead to a possible transient increase in $[O_2]$ in the pre-crack, with oxidation of ferrous ions to ferric and reduction in pH as a consequence of hydrolysis of trace amount of Fe^{3+} ions [11]. These processes could enhance anodic dissolution, sufficient to stimulate the transition to stress corrosion cracking or to accelerate the growth rate. The observation that this was not apparent in every test suggests that the conditions developed were close to the threshold for this transition.

It is perhaps fortuitous that in seeking to obtain crack growth rate measurements, new pits did form during the testing in two specimens and evolved to stress corrosion cracks. This enabled a reasonable estimate of the crack growth rates but also provided insight into the SCC initiation process.

4.2 IMPACT OF RH AND CRACK DEPTH ON GROWTH RATE

The stress corrosion crack growth rates measured in the conditions of interest were observed to decrease with increased RH and, to an extent, with crack depth. The increase in RH from 40% to 60% and then 80% effectively dilutes the $[Cl^-]$ in the solution, and this is sufficient to explain the resulting reduction in crack growth rate. When the RH was reduced from 80% to 60%, which effectively increased the $[Cl^-]$ and reduced the salt film thickness, the growth rate of all specimens was consistently increased from about 1×10^{-12} m/s to about 5×10^{-12} m/s. This does suggest that very slow growing and possibly arrested cracks could be reactivated by a change in exposure conditions.

The effect of crack depth on crack growth rate is more complex. The data at an RH of 40% are not extensive enough to indicate whether the rate would have progressively decreased with depth after the initial increase. However, at an RH of 60% the trend for a decreased growth rate with increasing depth in each individual test is apparent in all three sets of data (Figures 25 and 27), though the variability from one test to another is such that there is no consistent limiting depth value. The mechanical driving force, i.e. stress intensity factor, increases with increased crack depth. However, this is outweighed by the decreasing electrochemical driving force as the crack develops, in a manner perhaps proposed for developing pits [11]. It may be inferred that SCC propagation under atmospheric conditions could be a partially self-stifling process, limited cathodically by deposited area of the droplet [12]. However, evidence of cracking failures in service [13], the limitations of laboratory testing with a controlled environment, and variability in results would caution against generalisation without more extensive investigation.

4.3 COMPARISON WITH PUBLISHED DATA

Data in the literature relating to stress corrosion crack growth rates of relevance to stainless steel canisters for nuclear waste containment have been summarised by Enos and Bryan [14]. Most of the test results relate to 304L SS but there are a few sets of data for 316L SS [14-18]. These data enable some useful comparisons, although to a limited degree. The results of Tani et al. [18] are most relevant as they are based on DCPD measurement of crack growth rates, rather than average crack growth rates as shown in the others [16, 17] (i.e. crack extension divided by total exposure time). In this case, measurements were made with compact tension (CT) specimens with artificial seawater solution deposited in the notch. The growth rate was reported [18] to be less than 1×10^{-12} m/s at 50 °C and 35% RH (cf. Figures 25 and 27 at 40% RH, where much faster growth rates were measured). Crack growth rate data at 80 °C (up to 3×10^{-10} m/s at 35% RH) indicated a decreasing growth rate with time, consistent to an extent with observations in the present investigation. It is notable that the crack front shown for testing at 80 °C, for which the growth rate was more rapid, was very non-uniform in length with little propagation in some areas [18]. This raises a question about the analysis of data for that case, but even more so for the testing at 50 °C for which the crack extension would have been much less.

Cook et al. [17] undertook exposure tests of 316L SS U-bend specimens with deposited droplets of artificial seawater or $MgCl_2$ at varying concentrations and with temperatures of 40 °C (RH 33%), 60 °C (RH 26.5%) and 80 °C (RH 30%). Cracking was apparent at 80 °C (tests at lower temperatures were reported as ongoing), with the growth rate decreasing with exposure time. The initial (highest) average crack growth rates were reported as follows: for seawater and for seawater diluted 10 times the value was 1.4×10^{-9} m/s; for seawater diluted 100 times, the value was 1.8×10^{-10} m/s; for $MgCl_2$ at 0.3 M, the growth rate was 1.2×10^{-9} m/s. In all cases, the crack growth rate decreased with exposure time. In view of the higher temperature, direct comparison with our results is not meaningful at this stage.

Kosaki [16] tested a 316LN SS under 3-point bend loading with a through-thickness crack or with a half-elliptical surface crack. Natural exposure tests were conducted at Miyakojima Island, one of the most severe corrosive areas in Japan, and also in an environment filled with NaCl steam mist (95% RH)

at 60 °C as an acceleration test. No crack monitoring was undertaken, and the growth rate determined based on the crack extension divided by the exposure period. No cracking was observed for the base material under natural exposure condition but welded material did exhibit crack growth with growth rates ranging from 2.6×10^{-12} m/s to 2.1×10^{-11} m/s. For the accelerated test conditions the crack growth rate for the base material was 1.4×10^{-10} m/s and for the weld 5.0×10^{-11} m/s.

It is a feature of existing studies of stress corrosion crack growth rates that there is seldom overlap of test conditions in terms of salt characteristics, RH, temperature, specimen type, testing methodology. The consequence of this is that meaningful comparison of data across different studies is currently a challenge.

For this particular application of storage material for HAW, the use of $MgCl_2$ as the primary salt, the relatively higher temperature as an upper bound limit of storage environment, has been very effective in producing SCC initiation and propagation despite the moderately severe exposure conditions relative to the real storage environments. The current work has reassured confidence in the test method development, and also provides benchmarking data for any future comparisons of data in more realistic environments. With respect to the latter, a large variation in the characteristics of the chemical composition of the deposits on storage containers is expected, dependent on the location and storage housing. The focus going forward should be to identify what constitutes a feasible worst case deposition chemistry, to undertake appropriate testing to assess whether cracking does initiate, and to quantify the crack growth rate. The temperature and RH and its variation during the storage also needs to be accounted for.

4.4 IMPLICATIONS OF TESTING EXPERIENCE FOR TESTING METHODOLOGY

4.4.1 Indirect corrosion effects

Evidence of corrosion around and between the DCPD probes was observed for all specimens, with two consequences:

Corrosion can be detrimental to DCPD probe durability. The Pt probe connection can be gradually undermined by corrosion, which can lead to detachment of the probe from the surface. At that stage, no DCPD signal would be acquired and the test would be invalidated. In this work, the survival rate of DCPD probes was found to be 60%, which is unsatisfactory.

For the surviving DCPD probes, loss of material by corrosion between the probes can lead to a small increase in the measured potential drop (as detailed in section 3.3.1), which needs to be considered in decoupling from the increased potential drop associated with crack development. However, the magnitude of the potential drift induced by corrosion reduces progressively with time as the corrosion rate decreases and the relative effect will become progressively insignificant. At short testing times, however, the potential drift could be equivalent to a notional equivalent growth rate as high as 3×10^{-12} m/s and this needs to be factored in when interpreting the potential drop variation with time at the early stages of exposure.

4.4.2 Use of pre-crack as a SCC precursor

Fractography analysis revealed that the fatigue pre-cracking, which was originally designed to serve as a crack precursor, did not, in most cases, behave as a favoured site for SCC initiation and propagation. Among the three pre-cracked specimens that showed reliable DCPD signals (specimens AFUU7, AFUU12 and AFUU9), only specimen AFUU12 exhibited SCC and seemingly only in response to a system perturbation. In contrast to the pre-cracked specimens, two specimens (AFUU22 and AFUU15) developed new pits after the test started, which then transitioned to cracks. The crack propagation in both cases was much more substantial than that associated with the pre-cracked (specimen AFUU12). Hence, while the pre-cracking methodology may have been successful in other

applications, it would appear that pitting and pre-cracking does not create favourable conditions for development of a stress corrosion crack in the 316L SS under atmospheric corrosion conditions.

5 CONCLUSIONS

SCC propagation rates of 316L stainless steel in atmospheric conditions at 40 °C under $MgCl_2$ deposits (nominal CCD = 100 μg cm^{-2}) and at different RH (40%, 60% and 80%) were successfully measured with the DCPD technique at applied stresses of the order of 1.1 $\sigma_{0.2}$. Although the test duration, in each regime, may have been too short to determine long-term propagation rates, preliminary rates were obtained for an initial consideration of their likely impact. Specific conclusions that can be drawn from this study are as follows:

- The application of pre-pitting and pre-cracking as a precursor to development of stress corrosion cracks proved relatively ineffective in atmospheric corrosion conditions, at least for 316L SS. New pits generated during testing led more readily to the transition to stress corrosion cracking, which was attributed to a combination of a more aggressive local chemistry and dynamic plastic strain associated with the growing pit.
- Stress corrosion cracks exhibited a distinct fracture surface with a high density of fissures parallel to the stress axis, which is considered to be most likely attributable to preferential attack of delta ferrite.
- An increase in potential drop associated with mass loss due to corrosion was identified and introduced some uncertainty in the interpretation of the potential drop measurements at short exposure times. At long times, the effect diminished, consistent with the expected reduction in corrosion rate with time.
- An uncontrolled excursion of RH from 40% to 5% between the exposure period of 1445 h and 1704 h, caused a drying and rewetting of the $MgCl_2$ deposits, which led to a significant increase of SCC crack growth rate in two tests (Specimen 12 and Specimen 22). In the pre-cracked Specimen 12, stress corrosion cracking appeared to be initiated following the excursion. By implication, a drying and rewetting process, with $MgCl_2$ contamination, represents a severe exposure condition for SCC.
- There is unavoidable uncertainty in the calculation of the crack growth rate from the potential drop measurements when the crack depth was small, but there is confidence in the following statements.
- For RH values of 60% and 80%, the stress corrosion crack growth rates tended to decay with increasing crack length, consistent with the concept of limiting cathodic current supply in atmospheric conditions. Insufficient data were available at 40% RH to assess the long-term trend at that RH value.
- The estimated SCC propagation rates for different RH regimes were as follows:
    - At 40% RH, the growth rates attained values of 10^{-10} m/s (3.2 mm/year)
    - When increasing the RH from 40% to 60%, the crack growth rate decreased to about 10^{-11} m/s (320 μm/year) over a period of 2.5 months
    - Upon increasing the RH to 80% the crack growth rate decreased to about 10^{-12} m/s (32 μm/year) after 2 months
    - Decreasing the RH from 80% to 60% resulted in an increase in crack growth rate to about $3\text{-}5\times10^{-12}$ m/s (96-160 μm/year)

6 FUTURE WORK

The work presented in this study, exploring the application to atmospheric conditions of a methodology previously developed to study SCC in immersed conditions, was successful in providing reliable initial estimates of stress corrosion crack growth rates in the conditions of interest. Further work with a similar but improved methodology could be carried out to explore stress corrosion crack

propagation rates in conditions more representative of realistic storage environments, including tests with NaCl and/or at lower temperatures and CDDs.

Additional work could also be used to explore in more detail corrosion mechanisms occurring in the system of interest, including investigation of the morphology of attack (elongated fissures), and research to rationalise the impact of system variables on SCC initiation and propagation.

A strengthened testing methodology based on the lessons learned in this investigation would ensure more extensive and reliable test data for the wider range conditions to be explored leading to greater efficiency in testing. Specific improvements would include the following:

- Developing a more reliable DCPD probe connection without too much disturbance of local droplet chemistry. For example, placing the DCPD probes outside the droplet will mitigate corrosion attack at the probes and give more system reliability. The increased probe spacing will limit the measurement resolution of the DCPD system. Hence, some sacrifice in resolution would ensue but for this application the associated uncertainty in crack size determination would be relatively small and offset by greater reliability in the measurements.
- Undertaking crack growth rate measurement without pre-pitting and/or pre-cracking is recommended. Placing the probes outside the droplet zone will reduce some of the uncertainty associated with the pit and cracks formed during the test from developing too close to the probe. There is an issue in discriminating the growth rate of the pit from that of the crack but in an engineering context, this uncertainty is not significant.
- The salt deposition technique could be improved in order to minimize the variability and inaccuracy in CDD and heterogeneous salt distribution on surface induced by variation of surface wetness properties. The use of a technique relying on "instant" evaporation of a methanolic solution by depositing the solution on a heated specimen will be explored as a more effective alternative (see for example [19]).

7 ACKNOWLEDGEMENTS

This work is funded by Radioactive Waste Management Ltd.

8 REFERENCES

1. C. Padovani, O.E. Albores-Silva, and E.A. Charles, *Corrosion Control of Stainless Steels in Indoor Atmospheres-Laboratory Measurements Under $MgCl_2$ Deposits at Constant Relative Humidity (Part 1).* Corrosion, 2015. **71**(3): p. 292-304.

2. A. B. Cook, S. B. Lyon, N. P. C. Stevens, M. Gunther, G. McFiggans, R. C. Newman and D. L. Engelberg, *Assessing the risk of under-deposit chloride-induced stress corrosion cracking in austenitic stainless steel nuclear waste containers.* Corrosion Engineering Science and Technology, 2014. **49**(6): p. 529-534.

3. F. King, C. Watson, S. Watson, R. Metcalfe, J. Burrow, *The Atmospheric Corrosion of Stainless Steel in Stores (ACSIS) Model*, Quintessa Technical Report 17391-TR-010 Issue 2, 2016.

4. S. Zhou and A. Turnbull, *Influence of pitting on the fatigue life of a turbine blade steel.* Fatigue & Fracture of Engineering Materials & Structures, 1999. **22**(12): p. 1083-1093.

5. A. Turnbull, S. Zhou, N. McCormick, and M. Lukaszewicz, *An Approach to Measurement of Environmentally Assisted Small Crack Growth*, in *CORROSION 2013*. 2013, NACE International: Orlando, Florida. Paper No. C0002122.

6. R. P. Gangloff, D. C. Slavik, R. S. Piascik, R.H. Van Stone *Direct Current Electrical Potential Measurement of the Growth of Small Cracks* in *Small Crack Test Methods, J. M. Larsen and J. A. Allison, Editors, 1992, ASTM STP*.

7. S. Zhou, M. Lukaszewicz, and A. Turnbull, *Small and short crack growth and the solution-conductivity dependent electrochemical crack size effect.* Corrosion Science, 2015. **97**: p. 25-37.

8. ISO 12108:2012, *Metallic materials - Fatigue testing - Fatigue crack growth method*, BSI, 2012.

9. A. Turnbull, *Corrosion pitting and environmentally assisted small crack growth.* Proceedings of the Royal Society A: Mathematical, Physical and Engineering Sciences, 2014. **470**(2169): p. 20140254.

10. H. B. Mohammed-Ali, S. Street, M. M. Attallah, A. J. Davenport., *Effect of Microstructure on the Morphology of Atmospheric Corrosion Pits in Type 304L Stainless Steel.* CORROSION, 2018. **74**(12): p. 1373-1384.

11. A. Turnbull, *The solution composition and electrode potential in pits, crevices and cracks.* Corrosion Science, 1983. **23**(8): p. 833-870.

12. M. T. Woldemedhin, M.E. Shedd, and R.G. Kelly, *Evaluation of the Maximum Pit Size Model on Stainless Steels under Thin Film Electrolyte Conditions.* Journal of The Electrochemical Society, 2014. **161**(8): p. E3216-E3224.

13. J. Lieberzeit, T. Prosek, A. Jarvis, L. Kiener, *Atmospheric Stress Corrosion Cracking of Stainless Steel Rock Climbing Anchors, Part 1.* CORROSION, 2019. **75**(10): p. 1255-1271.

14. D. Enos, and C. R. Bryan, *UFD Expert Panel on Chloride Induced Stress Corrosion Cracking of Interim Storage Containers for Spent Nuclear Fuel*, Sandia National Laboratory, United States. doi:10.2172/1505413. https://www.osti.gov/servlets/purl/1505413.

15. K. S. Masumi Wataru, J. Tani, H. Takeda, S. Eto and T. Fujii. *Studies on the Long-term Integrity of the Canister for the Dry Storage of Spent Nuclear Fuel*. in *11th International Conference on the Transport, Storage and Disposal of Radioactive Materials*. 2018. London, United Kingdom

16. A. Kosaki, *Evaluation method of corrosion lifetime of conventional stainless steel canister under oceanic air environment.* Nuclear Engineering and Design, 2008. **238**(5): p. 1233-1240.

17. A. Cook, Stevens, N., Duff, J., Mishelia, A., Leung, T. S., Lyon, S., Marrow, J., Ganther, W., Cole, I., *Atmospheric-induced stress corrosion cracking of austenitic stainless steels under limited chloride supply*, Proceedings 18th International Corrosion Congress, Perth, Australia 2011.

18. J. I. Tani, M. Mayuzumi, T. Arai, N. Hara, *Stress corrosion cracking growth rates of candidate canister materials for spent nuclear fuel storage in chloride-containing atmosphere.* Materials Transactions, 2007. **48**(6): p. 1431-1437.

19. J. Rausch, S.G. Dorman, and S. Fawaz, *Test Methodology for the Investigation of Environmental Effects on Corrosion Fatigue.* CORROSION, 2019. **75**(5): p. 525-535.

APPENDICES

1 RAW DATA FROM DCPD MEASUREMENTS

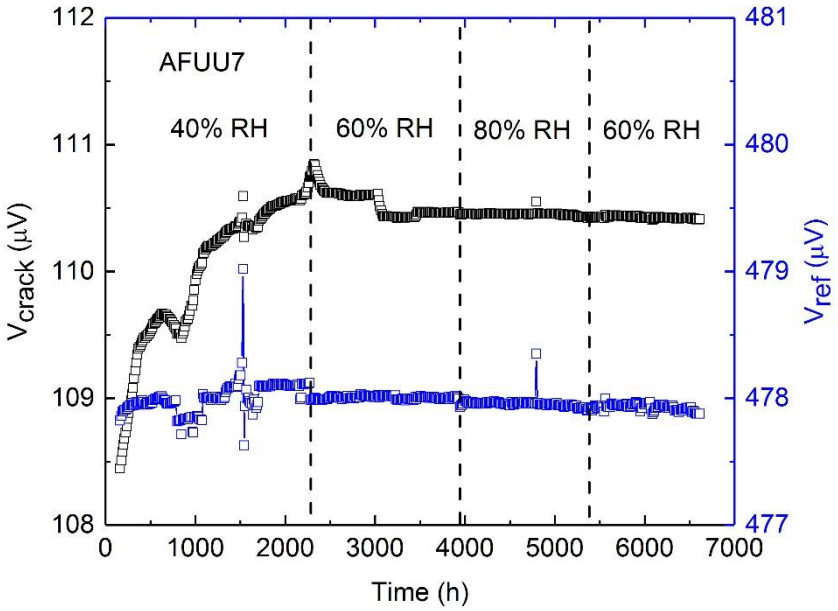

Figure A1. Potential drop (V_{crack}) and reference potential (V_{ref}) of specimen AFUU7.

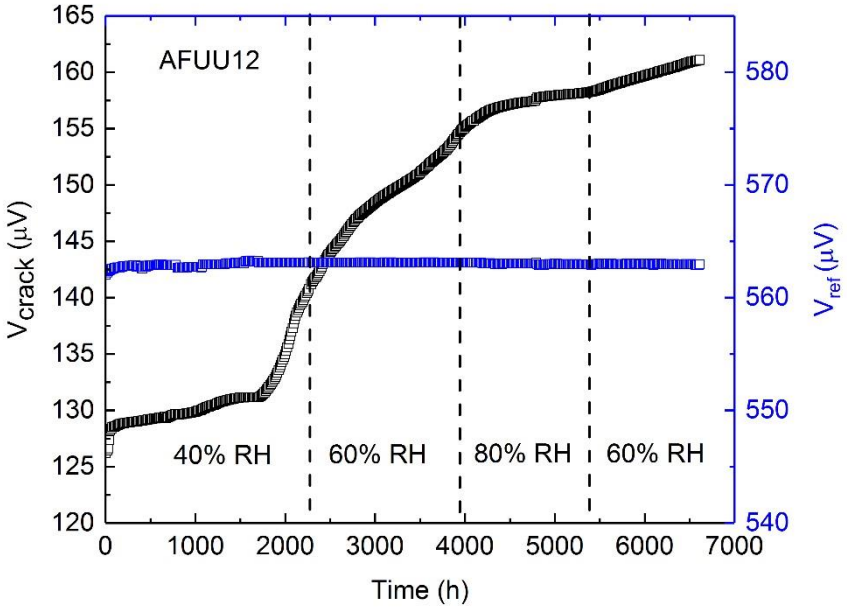

Figure A2. Potential drop (V_{crack}) and reference potential (V_{ref}) of specimen AFUU12.

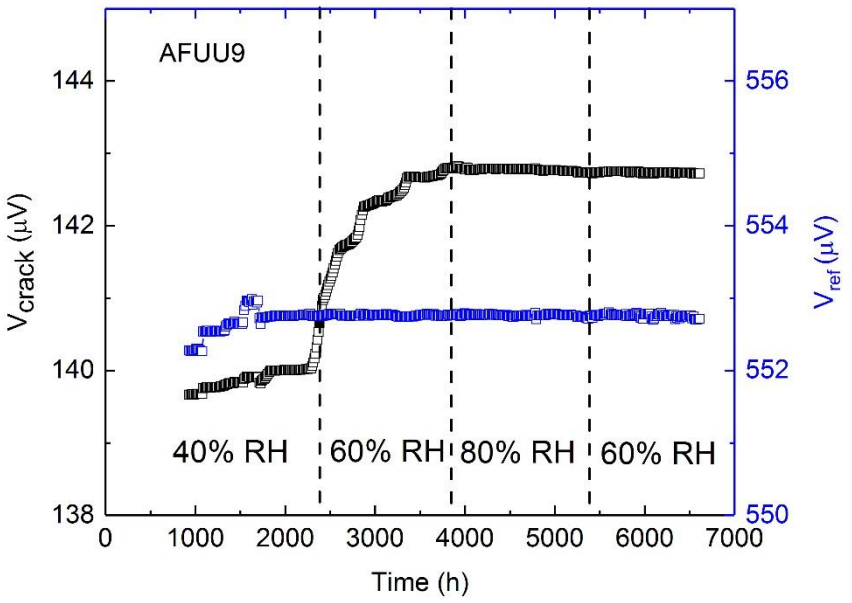

Figure A3. Potential drop (V_{crack}) and reference potential (V_{ref}) of specimen AFUU9.

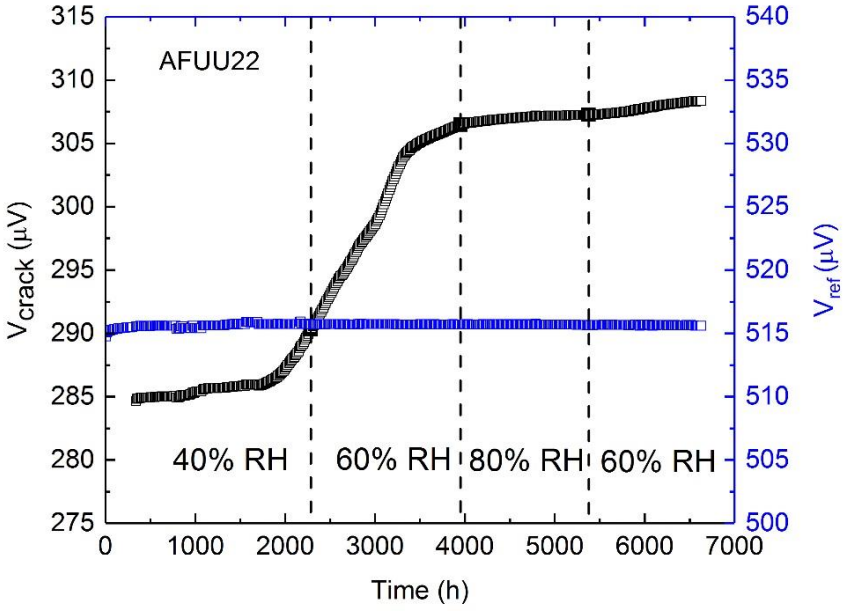

Figure A4. Potential drop (V_{crack}) and reference potential (V_{ref}) of specimen AFUU22.

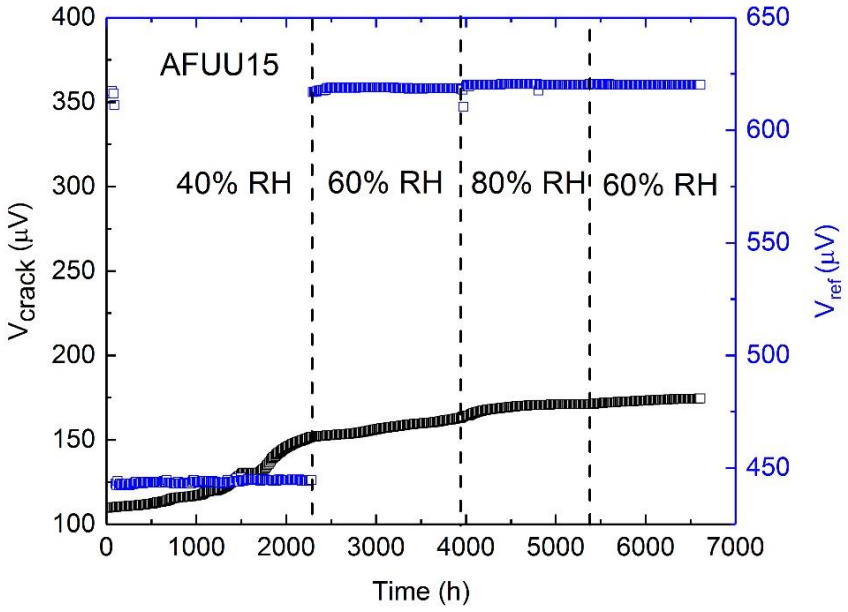

Figure A5. Potential drop (V_{crack}) and reference potential (V_{ref}) of specimen AFUU15. The change in V_{ref} at 40% RH was likely due to a faulty probe connection as there is no associated change in exposure environment and other tests in parallel showed no indication of such variation in V_{ref}.

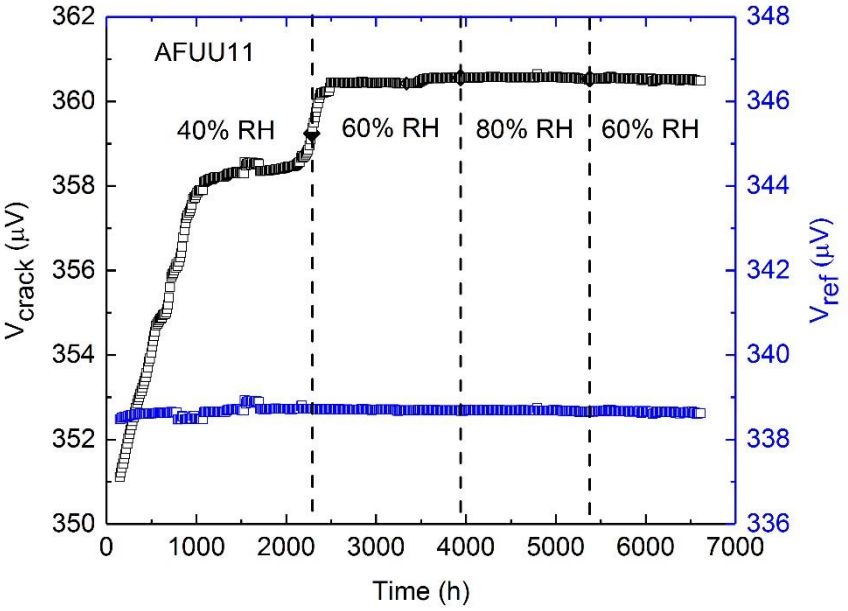

Figure A6. Potential drop (V_{crack}) and reference potential (V_{ref}) of specimen AFUU11. For specimen AFUU11 the spot-welded probes failed due to corrosion. New probes were attached at greater separation distance (1.5 mm compared with original spacing of 400 μm). Increased probe separation increases the magnitude of potential drop, increases the signal to noise ratio and reduces the voltage sensitivity to small changes in the crack size. Hence, in this test, although seemingly the potential drop signal increased, no discernible evidence of SCC was observed.

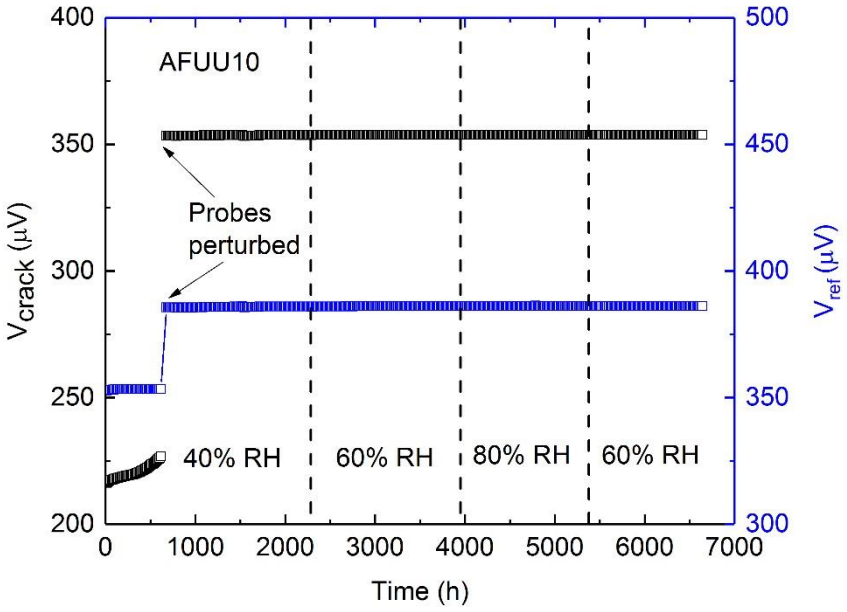

Figure A7. Potential drop (V_{crack}) and reference potential (V_{ref}) of specimen AFUU10.

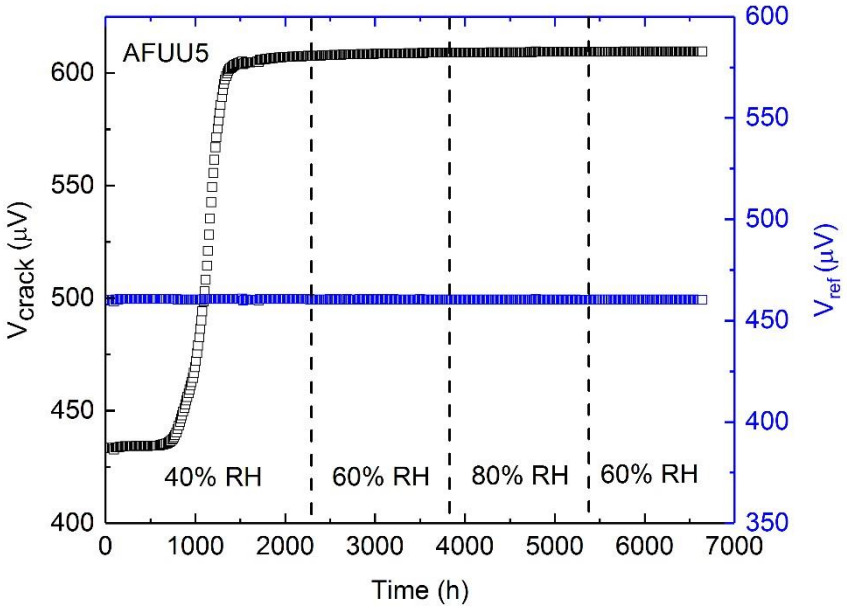

Figure A8. Potential drop (V_{crack}) and reference potential (V_{ref}) of specimen AFUU5.

2 COVERSION OF DCPD DATA TO CRACK DEPTH

The conversion from potential drop to crack depth in 3D surface cracks involves a complex analytical relationship developed by Gangloff et al., the details of which can be found in [6]. There are three key variables that must be input: the spacing between the centre position of the probes (L_p), the crack aspect ratio (a/c), and the initial crack size (a_n, b_n and c_n). The parameter b_n (crack opening or width) in the relationship can be considered reasonably as zero). Approaches are presented for conversion of potential to crack depth for two different crack growth scenarios: 1) initiation from the pre-crack (i.e. the initial crack depth is known) and 2) initiation from new pit formed during the test (i.e. the initial crack depth is unknown). The 'initial' term here refers to time zero, at which potential drop measurement was initiated.

For Case (1), the measured initial crack depth, a_n, is correlated with the first potential measurement V_c at time zero, $V_{initial}$. Together with the probe spacing L_p and a value for $(a/c)_{initial}$, as additional input parameters, the relationship of Gangloff et al. is then used to convert the voltage measurements as a function of time to a crack depth-time variation.

For this application, the final crack front shape was optimally fitted to an elliptical shape and the associated a/c value for the final crack size then adopted for all crack depths, including the initial value, $(a/c)_{initial}$. The computed final crack depth from the voltage signal conversion is then compared with the measured crack depth and should be in reasonable agreement. In practice, even with a crack with a well-defined crack shape, as in fatigue crack propagation, there can be small differences in measured and predicted value. The difference can arise because of uncertainty in the exact value of L_p, which relates to what constitutes the effective centre of the finite diameter (0.1 mm) spot-welded Pt probe on the specimen (see Figure B1). The approach adopted is to iterate around reasonable input values of L_p close to the initial assumed value until agreement between predicted and measured final crack depth is achieved. That value of L_p (typically within 20% of initial measured value) is then fixed and the full conversion of all potential drop values to crack depths can proceed with some degree of confidence.

The adoption of the measured a/c for the final crack for all crack depths including the initial value reflects the observation that stress corrosion crack evolution from a fatigue pre-crack does not proceed uniformly from the pre-crack with a well-defined aspect ratio. In fact, neither corrosion fatigue nor stress corrosion crack develop uniformly from a 3D pre-crack in the early stages. There is a period of early development when the crack has evolved only partially along the pre-existing crack front and the value of a/c is changing. There is no way to account for this in crack growth rate determination in the absence of crack front marking, but to simply recognise that the crack growth rates estimated for the early stage of crack development will have uncertainty. While recognising that uncertainty in crack growth rate for small cracks, the benchmarking against the measured final crack depth and shape gives confidence that the uncertainty in the crack growth rate will diminish with crack depth.

For Case (2) where the crack emerged from a new pit but not from the pre-crack or pre-pit, the assignment of initial voltage to an initial defect size and shape presents more of a challenge. The evolving pit contributes to potential drop in the early stages. Additionally, the potential drop associated with the transition from a pit to a crack with a crack front fully developed beyond the pit is also unknown.

The approach adopted for this case was to treat the growth of the pit as the growth of a crack-like defect, with the width b_n as zero, and to assign arbitrary small values to the initial crack depth, a_n, e.g. 5 µm, at test commencement. These assumed values are then correlated with the measured initial potential drop ($V_{initial}$). The same procedure adopted for the precrack case is then followed. The evolving crack shape at different crack depth is assumed unchanged and is based on the final crack shape as per measurement. Using the assumed initial defect parameters as above, and an initial value for the measured probe spacing, a projection of crack depth variation with time is produced. Any deviation from the predicted and measured final crack depth is corrected by small, realistic, adjustments of the probe spacing. Using the optimum value of the latter, the crack depth variation with time is predicted. In view of the arbitrary

nature of the initial defect size and lack of specific consideration of the pit, a sensitivity analysis was undertaken with varying values of the initial defect dimensions that are reasonably small (e.g. 5 - 40 µm, Figure B2) at test commencement. As expected, the variability in the predicted crack depth is small. In excess of about 100 µm, the differences in projection of crack depth at different arbitrary initial depths are minimal, suggesting the sensitivity to the initial conditions at greater depths is very low. Nevertheless, the apparent accelerated crack growth rate at the early stages is likely an effect of treating the 3D pit as a 2D crack.

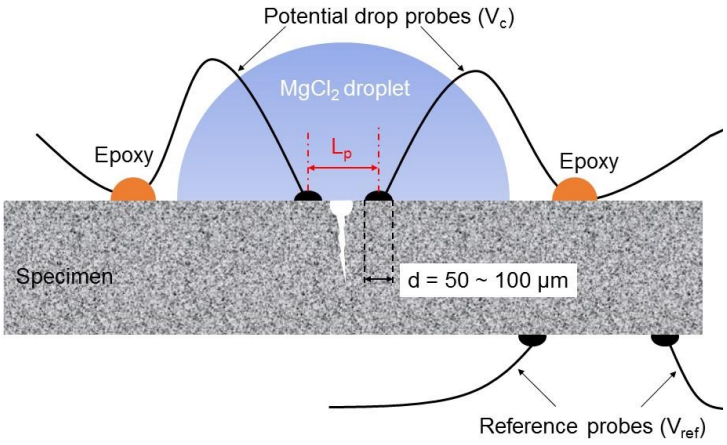

Figure B1. Schematic of position and spacing of DCPD probes relative to the crack and droplet. The thickness of salt film may change with varying RH conditions.

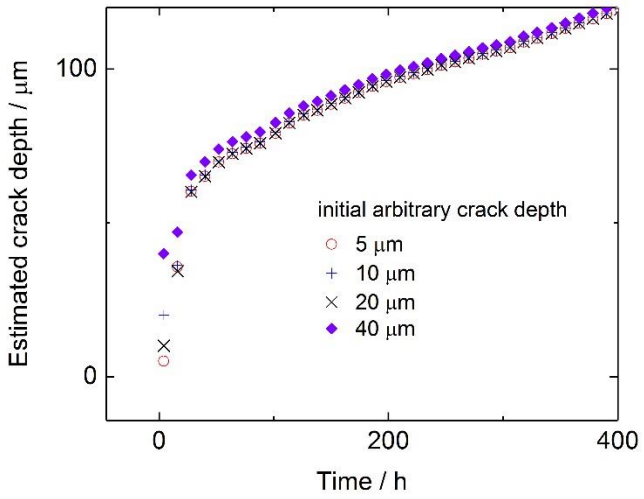

Figure B2. Estimated crack depth of Specimen AFUU15 based on different assumed initial defect size; namely 5 µm, 10 µm, 20 µm, 40 µm.